Development of Dynamic Centrifuge Models for Measurement and Visualization of Deformation Mechanisms in Liquefiable Soils

Caroline Bessette[1], Lianne Brito[2], Shideh Dashti[3], Abbie B. Liel[4], Brad P. Wham[5]

ABSTRACT

Recent advancements in geotechnical physical modeling have enabled visualization and analysis of deformation mechanisms in soil sections through the integration of Particle Image Velocimetry (PIV) in dynamic centrifuge modeling. PIV requires a rigid wall container. In this paper, we summarize the design considerations that enable reliable measurement and visualization of soil deformation mechanisms at the University of Colorado (CU) Boulder's 400g-ton, 5.5 m radius centrifuge facility. The primary objective of this system is to investigate the response of complex and stratigraphically variable, saturated granular soil deposits beneath shallow-founded structures, though it can also be used for other configurations that benefit from advanced visualization in the centrifuge. The setup aims to enable quantification and visualization of different deformation mechanisms, including shear, volumetric, and soil ejecta formation, near and away from structures. The paper provides detailed design considerations for the system components, including a rigid container with a transparent Perspex wall and duct seal inclusions, a linear-elastic single-degree of freedom (SDOF) structure, soil texture, a potential ground improvement technique, and a high-speed camera system. Through fully-coupled, three-dimensional (3D) nonlinear finite element analyses, we investigate the influence of container type, domain size, and duct seal geometry on boundary effects, with consideration of nonlinearities within various soil profile configurations with and without the presence of a building model. The findings highlight the critical impact of proximity to lateral boundaries of the container on accelerations, excess pore pressures, foundation settlement, tilt, and shear strains, as well as the benefits of duct seal in

[1-5] Department of Civil, Environmental, and Architectural Engineering, College of Engineering and Applied Science, University of Colorado Boulder, 1111 Engineering Drive, Boulder, CO, 80309, USA
*Corresponding author.
E-mail addresses: caroline.bessette@colorado.edu (C. Bessette), lianne.brito@colorado.edu (L. Brito), shideh.dashti@colorado.edu (S. Dashti), abbie.liel@colorado.edu (A.B. Liel), brad.wham@colorado.edu (B.P. Wham)

reducing those boundary effects. The results also show that the extent of boundary effects on key performance measures depends on the properties of the container, soil layers, and ground motion. The simulations also show that surface ejecta potential within stratigraphic soil profiles is highly sensitive to the depth of the groundwater table and variations in soil permeability, which must be considered in designing experimental programs that investigate the development of soil ejecta.

Keywords: Centrifuge Modeling, Liquefaction, Particle Image Velocimetry (PIV), Boundary Effects, Soil-Structure Interaction

1 INTRODUCTION

Past earthquakes have consistently shown the significant economic damage, loss of life and community disruption resulting from earthquake-induced soil liquefaction on the built environment. Centrifuge modeling is a cost-effective method to simulate the seismic response of scaled geotechnical problems under realistic confining pressures, while also aiding in the validation of numerical models used in design. Here, we explore the developments needed in centrifuge modeling to examine the interaction of deformation mechanisms between the soil and surrounding structures, for which the underlying physics is poorly understood.

Recent developments include the Particle Image Velocimetry (PIV) technique, which utilizes high-frame-rate cameras, to visualize deformation mechanisms within visible soil sections during dynamic centrifuge testing (Adamidis and Madabhushi 2018). The PIV technique often requires a rigid container with a transparent window. However, such containers can introduce large boundary effects compared to other container types commonly used in dynamic centrifuge testing, such as laminar or flexible shear beam (FSB) containers. These adverse effects can be reduced by including Duct Seal (DS) inclusions to the sidewalls of the rigid container, as quantified by Cheney et al. 1998 and Steedman and Madabhushi (1991).

Saturated granular sand deposits susceptible to liquefaction often show stratigraphic variations in the ground slope or soil layer thickness, permeability, and relative density (Ishihara 1985; Kokusho and Fujita 2001; Badanagki et al. 2019). Recent investigations have shown that even minor variabilities in these properties significantly affect the surface manifestation of liquefaction, soil deformations, and

subsequent damage to overlying structures (Badanagki et al. 2018; Beyzaei et al. 2018a,b; Luque and Bray 2017; Paramasivam et al. 2018). Additional experimental studies employing PIV are warranted to characterize the deformation mechanisms in interlayered deposits at a systems level, both near and away from structures. Furthermore, a deformation measurement system integrating PIV proves valuable in various other applications within geotechnical engineering, such as seismic soil-structure-interaction (SSI), ground improvement techniques, buried structures, and embankments.

This paper presents the development of a deformation measurement system that enables reliable measurement and visualization of deformation mechanisms in liquefiable soil deposits in the far-field and near a structure in a centrifuge using PIV techniques. The system is also applicable to other centrifuge applications. An overview of the conception and implementation of different experimental components designed at CU Boulder's 400 g-ton (5.5 m-radius) centrifuge facility is provided. We present the design considerations and assumptions for a model building structure, transparent rigid container equipped with duct seal, PIV system, and highlight potential application of the experimental set-up. Additionally, we use fully-coupled, three-dimensional (3D), nonlinear finite element (FE) analyses to quantify the boundary effects introduced by a rigid contained compared to other boundary types. A limited sensitivity study is then performed to investigate the influence of duct seal thickness, uncertainties in its properties, and distance to lateral boundaries on boundary effects.

2 DESIGN CONSIDERATIONS FOR A MODEL BUILDING STRUCTURE

The experimental setup described in this paper was intended to enable evaluation of seismic soil-structure interaction on highly stratified soil deposits. We describe the design considerations for an example model building structure that affected the design of the container and image capturing criteria. A similar methodology may be followed for other problems of interest (e.g., underground structures or other systems).

2.1 Design Criteria

The design of the building structure was governed by four main considerations. First, it was important to represent the key dynamic properties of a realistic prototype structure in a high seismic area. Second, the maximum dimensions of the building were affected by the size of the rigid container, practicality

considerations for the construction of and sensor installation around a scaled model, and the limitations imposed by the centrifuge overhead space. The total height of the simplified scaled structure was restricted to less than 250 mm in model scale (equivalent to 17.5 m in prototype scale) based on the designed container and selected soil profiles. The third consideration was to design a structure that would amplify soil-structure-interaction (SSI) and enable experimental evaluation of the variations in soil response in the near- and far-field. To achieve this, the design aimed for a bearing pressure exceeding about 70 kPa and a height-to-width (*H/B*) of around 1.5. These parameters were chosen to approximate the characteristics typically observed in 4-story buildings and were informed by previous case histories and experimental results that showed foundation damage on liquefiable soils (Dashti et al. 2010a,b; Sancio et al. 2004). Fourth, the foundation needed to be designed as a strip footing to maintain plane strain conditions and permit visualization of the soil deformations under 2D conditions in the new deformation measurement system. Accordingly, the structure-foundation system had to span the entire width of the container, ensuring a flush alignment against the Perspex window with a 2-mm thick neoprene foam strip of soft hardness placed on both sides of the foundation. This arrangement was needed to prevent sand particles from infiltrating the interface between the structure and the window during preparation and testing. The accuracy of particle tracking would be reduced if sand particles were to migrate through the front interface of the structure.

2.2 Selection of the Target Prototype Building

The target prototype 4-story reinforced concrete frame structure was selected from a database of buildings that experienced significant damage due to soil liquefaction during the Christchurch earthquake sequence, as documented by Zupan (2014). Some of the damage documented for this representative prototype included sediment ejecta within the building's footprint and parking lot, cracks on exposed concrete columns, and a differential settlement of 16 cm. To suit our experimental needs, the representative building was modified in two ways. First, the height of each floor was increased to achieve a slightly higher H/B ratio to amplify SSI effects. Second, the mass of the modified target building was increased by 50% to account for the typical design range of 586-684 kg/m^2 mass per story for concrete buildings (ASCE, 2013) in the U.S., accounting for the differences in floor construction

between the U.S. and New Zealand. Based on Goel & Chopra (1997), the estimated fundamental period range for a building of this height, featuring a concrete moment-resisting frame structural system, is 0.64 to 0.9 s. The design period value according to American practice (ASCE/SEI 7-22) is 0.64 s.

2.3 Design and Construction of the Simplified Scaled Model Structure

Table 1 and Fig. 2 present the target prototype structure and the simplified model, along with their key dimensions. Several simplifications were required to convert the modified target prototype structure into model-scale dimensions and simplify it for centrifuge testing at 70 g ($N = 70$). Table 1 summarizes the design properties and dimensions of the modified target prototype structure and the simplified centrifuge model, which was constructed from 6061-T6 aluminum alloy. The 4-story prototype structure was simplified and scaled as a single-degree-of-freedom (SDOF) oscillator. The effective height of the SDOF representation was taken as 70% of the total height of the modified target prototype (FEMA, 2005), which is 200 mm, in accordance with our height limit design criteria. A rigid mass at the roof level created a fixed-fixed condition for the "columns". These columns were thin in the direction of shaking and extended the entire dimension of the box's width (out of plane direction) (4.8 by 362 mm). The model column member sizes were determined from the target fundamental period and mass. The final design of the simplified model structure also took into account considerations such as the ease of constructability and the use of commercially available parts.

Once fabricated, the natural period and damping of the model structure, in a fixed-based condition, were determined through a series of impact hammer tests. The measured fundamental period agreed well with the value obtained from the Goel & Chopra (1997) upper limit equations, which was also well reproduced by the 2D OpenSees model (Mazzoni et al. 2006). The damping ratio of the simplified structure was computed as 0.2% using the logarithmic decrement method, which is on the order of that expected for metal structures with multiple bolted connections (Olarte et al. 2018).

The bearing pressure at the bottom of the foundation was calculated as 90 kPa based on its weight and footprint, and this value was verified with measurements. The simplified model structure was painted matte black to reduce glare from the LED lights. Additionally, a checkered pattern adhesive

with dots was applied to the structure to enable tracking of the movement of the structure with the PIV software during testing.

3 DESIGN OF THE CONTAINER AND DUCT SEAL INCLUSIONS

3.1 Rigid Container Design and Fabrication

In a prototype scenario, soil layering extends infinitely laterally, while a centrifuge model is constrained within a finite size and is bounded by stiff sidewalls. Bhattacharya et al. (2012) summarized the key objectives of designing a model container for dynamic geotechnical centrifuge testing. These objectives include achieving: 1) similarity between the model and prototype conditions in terms of stress and strain; 2) vertical propagation of shear waves (generated through base shaking) to the contained soil profile; 3) reduction in wave reflections from the sidewalls; 4) water tightness for saturated specimens; and 5) adequate lateral stiffness to maintain a near zero-lateral strain (K_o) condition or avoid approaching active (K_A) conditions. These objectives can be achieved through different types of containers, each with its own advantages and disadvantages. Common soil container types used in dynamic testing include: 1) Laminar containers; 2) Equivalent shear beam (ESB) containers; 3) Flexible shear beam (FSB) containers; 4) Rigid containers with hinged end-walls; and 5) Rigid containers with flexible boundaries such as Duct Seal or sponge. In order to benefit from the transparent side of a relatively long-span container for PIV with high-speed photography, we selected, designed, and constructed a rigid container.

The main limitations of rigid containers include excessive wave reflection from the rigid boundaries and constrained soil deformations (Bhattacharya et al. 2012). To alleviate these issues, Duct Seal (DS) can be applied to both end walls of the rigid box in the direction of shaking. The use of Duct Seal is expected to: partially reduce wave reflections (e.g., absorb 65% of incident waves), and decrease the lateral stiffness of sidewalls (Cheney et al. 1998; Steedman and Madabhushi 1991). Given the high compressibility of Duct Seal, Pak and Guzina (1995) observed deformations under centrifugal forces that led to non-homogeneity around the sides of the soil specimen. This issue was addressed by incorporating a supporting grid for Duct Seal boundary inclusions, providing greater lateral wall stiffness. In this study, the rigid box was slightly modified with an Aluminum panel and T-bar system

to support the boundary lining, while reducing the added wall stiffness and facilitating the construction process.

The inside dimensions (Length x Width x Depth) of the rigid container (without Duct Seal inclusions) were selected as 967 x 375 x 350 mm [model scale] (67.69 x 26.25 x 24.5 m [prototype scale]), as shown in Fig. 3a. This size was determined based on the limitations of the centrifuge platform in both plan view and headroom space and the payload capacity of the shake table. The selected container dimensions also helped minimize boundary effects near a structure placed at the center with its expected dimensions noted previously. Whitman and Lambe (1986) quantified the zones close to the end walls of a container that are affected by the artificial boundary under dynamic loading as those within about a distance of 1.5 times the depth of the soil profile. As a result, the target length-to-depth ratio (L/D) of the container needed to be greater than 3, to minimize boundary effects. A soil total depth (D) of about 18 m [prototype scale] (257 mm [model scale]) was anticipated, representing L/D = 3.8.

We designed the rigid container with three sides made of aluminum and one transparent Perspex wall along its length to maximize visualization opportunities within the soil. The front plate included two metal frames that enclosed the 76 mm-thick Perspex, to ensure better sealing and support.

Three-dimensional structural analyses using the finite element (FE) program ABAQUS (Simulia, Dassault Systèmes, Paris, France) were conducted to determine the appropriate sizes of the aluminum and Perspex sections, with the goal of limiting the maximum static lateral deflections along the container's mid-span when filled with saturated sand and subjected to the anticipated 70 g of centrifugal acceleration. The limiting deflection was taken as δ/H = 0.003 or δ = 1.2 mm for active conditions in loose sands (Das, 2016), where δ is the sum of the maximum lateral deflection from the front and back plates, and H is the total container height (400 mm in model scale from the top of the angle to the base plate). For design purposes, the aluminum and Perspex materials were assumed to remain linear-elastic (Table 2). The container was assumed to be filled with saturated sand to statically evaluate the lateral deflection profile along the height of the container.

The static lateral earth pressure was estimated in prototype scale based on a uniform sand layer with a saturated mass density of $\rho_{sat\text{-}soil}$ = 2000 kg/m^3, pore water mass density of ρ_{water} = 1000 kg/m^3, scaling factor N = 70, and K_o = 1 (assuming a temporarily liquid-like condition after soil liquefaction).

This lateral earth pressure calculation accounted for the structure's bearing pressure (90 kPa). The final design considered fixed boundary conditions on the side steel angles, which were to be bolted to the shake table. The numerical simulations produced a maximum deflection of 0.6 mm for the back aluminum plate and 0.4 mm for the front Perspex plate of the container mid-span, resulting in a total deflection of 1.0 mm in model scale (70 mm in prototype scale), corresponding to δ/H = 0.0025, as shown in Fig. 3b. These results adhere to our limiting deflection design criteria and represent a conservative estimate, because the planned centrifuge experiments will not fill the container with soil, the K_o = 1 assumption is highly conservative, and the analysis did not account for the presence of four steel instrumentation racks spanning the container's width, which restrict the lateral expansion of the box.

The base of the container was designed to enable rapid and automated saturation and drainage to accommodate studies of soil liquefaction. The base was equipped with four drainage holes (fluid inlet valves). Additionally, a series of 5 mm-high fluid gaps were incorporated along the bottom grid, below the porous stones, to allow the fluid to fill the space uniformly before saturating the entire specimen from the bottom up (similar to Paramasivam 2018 and Brennan & Madabhushi 2002). To ensure water tightness on all container surfaces, PORON AquaPro gaskets from Rogers Corporation were applied in areas where sealing was required. After the container was fully assembled, a coat of clear Flex Seal (a liquid rubber sealant) was applied along areas where leakage was observed, to ensure that the container was watertight.

3.2 Characterization of Boundary Effects and Duct Seal

After ensuring static deformations were acceptable, fully coupled, 3D, dynamic, effective-stress, FE simulations were performed in the object-oriented, parallel computation platform OpenSees to assess boundary effects and design the duct seal geometry in the transparent rigid container. Boundary effects were evaluated within the container for three soil profiles with and without a model building to represent the effects of container boundary conditions on soil-structure-interaction (SSI). The seismic performance of our rigid container with duct seal inclusions (rigid w/ DS) was compared to other boundary types, including rigid without DS and a Flexible-Shear-Beam (FSB) container with periodic

boundaries. The thickness of DS, domain size, and boundary type were varied to evaluate their influence on the seismic performance indices of interest within the soil-structure system through a limited sensitivity study.

3.2.1 Numerical Modeling Approach and Characteristics

3.2.1.1 Modeling of Soil and Structural Properties

A series of three soil profiles with a total thickness of 18 m were numerically simulated, as presented in Fig. 4b, based on container dimensions and the expected geometry of soil specimens. The first soil profile (Uniform dry – P1) consisted of a uniform layer of dry, dense Ottawa sand at a relative density (D_r) of 90%. Soil profile 2 (Uniform saturated – P2) comprised a uniform saturated layer of loose Ottawa sand with D_r = 40% prone to softening and liquefaction. Soil profile 3 (Layered saturated – P3) represented the baseline case for our intended series of centrifuge experiments, consisting of a 6 m-thick loose Ottawa sand layer (D_r = 40%) in the middle of 10 m and 2 m-thick layers of dense Ottawa Sand (D_r = 90%) at its bottom and top, respectively.

The pressure-dependent, multi-yield surface, version 2, soil constitutive model (PDMY02) implemented in OpenSEES by Elgamal et al. (2002) and Yang et al. (2008) was used to simulate the nonlinear response of all soil layers. PDMY02 is based on multiple yield criteria defined by several open conical-shaped yield surfaces with a common apex at the origin of the principal stress space, with different sizes that form the hardening zone (Yang and Elgamal 2000). This elastoplastic constitutive model uses the deviatoric kinematic hardening rule and follows a non-associative flow rule to simulate the soil's volumetric dilatation and contraction response under shear. In addition to the model's hysteresis damping, a small-strain Rayleigh damping value of 3% at frequencies of 2.3 and 11.4 Hz (corresponding to the soil column's first and third initial modes) was employed for all soil profiles, following a similar approach as in Hwang et al. (2021, 2022), Ramirez et al. (2018), and Kwok et al. (2007).

The model parameters used for the saturated Ottawa sand layers were adopted from Hwang et al. (2021) and Ramirez et al. (2018), as summarized in Table 3. These were calibrated to ensure that best-fitting parameters captured on average: (1) the fully drained or undrained monotonic and cyclic

triaxial element tests; (2) the empirical cyclic stress ratio (CSR) relationships to trigger liquefaction in 15 cycles (NCEER 1997); and (3) site response in a previous free-field boundary-value centrifuge test involving the same soil column and sequence of motions (Hwang et al. 2021). This calibration methodology using diverse data types is designed to achieve a balance between model precision and the potential impact of experimental errors. All soil parameters were calibrated for saturated conditions in previous studies. The same parameters were used for the dry soil at a corresponding D_r. A dry soil profile was included in this study due to a reduced degree of material damping compared to saturated states, which was hypothesized to amplify the influence of duct seal boundaries.

The dry and saturated soil domains were modeled using 3D, higher order, 20 node, standard brick elements and 20-8 node, two-phase, brick elements with a u-p formulation (Zienkiewicz et al. 1990), respectively. In the u-p formulation, the corner nodes of the elements had four-degrees-of-freedom (4DOF), one to represent the fluid pressure and 3 for solid displacements, while all other nodes had 3DOFs for displacement only. A water bulk modulus of 2.0 x 10^6 kPa was assigned to the fluid to simulate fully saturated conditions in soil profiles P2 and P3. The maximum allowable element size (hmax) was determined with depth based on the corresponding soil profile's empirical small-strain shear wave velocity (V_S) (Seed and Idriss 1970; Bardet et al. 1993; Menq 2003) and the maximum frequency content of the input motion in the centrifuge (e.g., estimated as f_{max} = 10 Hz in prototype scale). The minimum wavelength ($\lambda_{min} = V_S/f_{max}$) was divided by 4 to obtain hmax. Subsequently, hmax was further reduced by a factor of C = 4 to account for soil softening at large shear strains (i.e., reduction in V_S), such that hmax = $\lambda_{min}/4C$. The constant C was determined based on a sensitivity study of a free-field soil column (Ramirez et al. 2018; Hwang et al. 2021). Fig. 4c shows an example of the V_S profiles and element size distribution obtained for soil profile P3.

The soil domain was modeled to represent the inside dimensions of the container with appropriate boundary conditions. The distance from the foundation's edge to the lateral boundaries (L) (as illustrated in Fig. 4b) was 27 m, representing L/B = 2.7 (where B is the width of the foundation). A width of 1 m was selected into the page (perpendicular to the shaking direction), due to the 2D, plane strain nature of the problem.

For the case of a rigid container, the side nodes of the model were fixed in the *x* direction (Fig. 4a). Periodic lateral boundary conditions were assumed for the FSB container by tying the nodes at the same elevation in the *x*-*z* directions. The model's base nodes were fully fixed (i.e., *x*-*y*-*z* direction), and those at the soil surface had a prescribed zero pore pressure condition. Out-of-plane displacements were also restricted on both faces parallel to shaking (i.e., *y*-direction).

Three 1-D, horizontal earthquake motions for which the centrifuge shake table was calibrated were selected as the base motion for our simulations, representing a range of amplitudes, durations, and frequency contents. The acceleration and Arias Intensity (I_a) time histories and 5%-damped acceleration response spectra (S_a) of motions referred to as Kobe (M1), Joshua Tree (M2), and Northridge (M3) are presented in Fig. 5, along with their properties in Table 4. These motions were selected based on prior calibration of the shake table, to represent a range of amplitudes, durations, and frequency contents. The acceleration time histories were applied at both the base and side nodes for the rigid container and only at the base nodes for the FSB container.

In cases involving a model building in the center of the container (Fig. 4a-b), the foundation was modeled using 20-8 node brick elements with the u-p formulation and an embedment depth of 1 m. The fluid mass density of the foundation elements was set to 0, and the DOF for fluid pressure was fixed to avoid excess pore water pressure generation. The base and side nodes of the foundation were connected to the surrounding soil in all directions using a master/slave (equalDOF) connection. The base nodes of the foundation were fixed in all directions (i.e., *x*-*y*-*z*). The side nodes were fixed only in the two horizontal directions (i.e., *x*-*y*), allowing for movement of the foundation relative to the surrounding soil [similar to the approach taken by Karimi and Dashti (2016a-b), Shahir et al. (2016) and Hwang et al. (2021, 2022)]. The SDOF, plane-strain structure was modeled using a beam-column element assembly, which matched the stiffness, mass, and bearing pressure (q = 90 kPa). A Rayleigh damping formulation with a damping ratio of 0.2% was assigned to the structural elements at frequencies corresponding to the first and third modes of the structure. The structure elements were restricted from out-of-plane displacements. Given the incompatibility between the beam elements (6DOF) and the foundation elements (3DOF), a massless rigid beam element was used to connect the foundation to the structure's columns.

3.2.1.2 Modeling of Duct Seal

The duct seal was modeled using 20-8 node brick elements with the u-p formulation and prescribed zero pore pressures. The absorbing boundaries were simulated as linear-elastic following Kassas et al. (2021), Cilingir and Madabhushi (2011), and Chakrabortty and Popescu (2012). We used a Young's modulus of E = 800 kPa, a Poisson's ratio of v = 0.46, and mass density ρ = 1.65 Mg/m^3 for DS based on Popescu & Prevost (1993). In addition, material damping was introduced using the Rayleigh damping formulation (Cilingir and Madabhushi 2011; Pak et al. 2011). The selected damping ratio (ζ_{DS}) was based on resonant column tests, defined using Eq. (1) from Pak et al. (2011).

$$\zeta_{DS} = 0.18 - 0.0003 \times \left(\frac{\sigma_{mean}}{1\ kPa}\right) \quad (1)$$

The DS boundary was divided into sublayers of 2 m in thickness following the discretization of the soil domain, and the ζ_{DS} and mean total stress (σ_{mean}) values were calculated at the center of each sublayer. EqualDOF restrictions (i.e., *x*-*y*-*z*) were applied for the contact nodes at the soil-DS interface. Finally, a baseline DS thickness (w_{DS}) of 24 mm (25.4 mm in model scale or 1.7 m in prototype scale) was selected, similar to other dynamic centrifuge studies (e.g., Adamidis 2017).

We acknowledge that sources of uncertainty particularly in DS properties might influence the results obtained from this numerical study. As such, we performed a sensitivity study (see Appendix A) to evaluate the influence of DS' Young's Modulus (E) from 400 to 1600 kPa and Rayleigh damping formulation on the response parameters of interest in the soil-structure system (as noted influential by Kassas et al. 2021). In general, for the soil profiles and ground motions investigated, and a reasonable range of E, the influence of E on accelerations, permanent foundation settlement, shear strain contours, and excess pore water pressures was not significant. For example, the permanent foundation settlement and soil excess pore pressures showed a difference ranging from 0 to 7% (average of 2%) and 0 to 15% (average of 4%), respectively, for the range of E values considered for DS. The difference in *PGA* at various locations within the container (e.g., at a distance of *L/2* from the foundation edge, under the building, and on the foundation) ranged from 2 to 22% (average of 11%) for different E values. The influence of E of DS was more notable on the foundation's permanent tilt, with a difference of 1 to 162% (average = 32%). However, the tilt values were generally negligible in this case, as is expected

for isolated and symmetric structures on uniform liquefiable layers (see Bullock et al. 2019b), and these small values led to the calculation of larger percent differences. Nevertheless, we acknowledge that the idealization of duct seal as a linear elastic material is simplistic and should be further verified.

3.2.1.3 Benchmark Container: Idealized Laminar Container

An Idealized Laminar Container (ILC) was used as a benchmark case for comparison with the newly designed container. The ILC was first proposed by Kassas et al. (2021) to simulate free-field conditions (i.e., infinite boundaries). The boundary effects were minimized in ILC by using periodic boundaries and a soil domain of sufficient size in 3D. In this study, different domain sizes (L/B = 15, 25, 35, 45) were tested by varying L while keeping all other dimensions constant. We set the smallest domain to L/B = 15, given that the structural response (e.g., foundation settlement and tilt) and excess pore water pressure values under the building were shown to converge with these boundary distances (e.g., see Figure 7efg). The largest domain was set to L/B = 45 to limit the computational cost. We subsequently selected the ILC domain size through a sensitivity study and comparison of the ILC far-field response in terms of spectral accelerations with 3D simulations of single soil columns (SSC). Residuals in the 5%-damped acceleration response spectra (S_a) were computed as defined in Eq. (2), with respect to the SSC results.

$$S_{a-Res}(T) = ln[S_{a-SSC}(T)] - ln[S_{a-ILC}(T)] \quad (2)$$

Fig. 6 presents the average S_a residuals for all three soil profiles and motions in the middle of the liquefiable layer (or middle of the dense layer for soil profile P1) at a lateral distance of $L/2$ from the container side boundaries and the foundation edge (as illustrated in Fig. 4b) as well as the middle of the container in plan view, both with and without a building, respectively. Overall, the largest domain (L/B = 45) led to the best approximation of the peak ground acceleration (PGA) and accelerations at T > 3 s in the far-field compared to SSC across other tested domains with L/B = 15, 25, 35. Therefore, with satisfactory predictions of accelerations, excess pore pressures, and displacements at key locations, L/B = 45 was selected as the ILC.

3.2.2 Influence of Domain Size and Boundary Type on System Performance

In this section, a limited sensitivity study is performed to evaluate the effects of domain size on boundary effects within different soil-structure-container systems. Three container types were considered in this sensitivity study: i) a rigid container without DS, ii) a rigid container with DS, and iii) an FSB container with periodic lateral boundaries and no DS. The distance from the foundation edge to the container sides (L) was varied from L/B (Fig. 4b) = 1 to 15. The response in the containers was compared to ILC using the previously identified seismic performance indices averaged for motions M1-M3 considering soil profiles P1 and P3. The SDOF structure (B = 10 m, q = 90 kPa, H = 9.8 m) was included in the center of the container for all the analyses.

Fig. 7 shows the Root-Mean-Squared-Error (RMSE) of spectral accelerations determined numerically at different locations (i.e., between each container and the ILC). This figure illustrates that, for soil profile P3, the periodic lateral boundaries (i.e., in an FSB container) were the most effective in reducing boundary effects (in terms of RMSE of S_a) for smaller domain sizes ($L/B \leq 2.7$). The rigid container with DS only offered a slight improvement for smaller domain sizes compared to the case without DS, as the proximity of rigid boundaries limited the deformation mechanism from developing fully. Overall, the performance of all boundary types appeared to converge for a domain size $L/B > 4$ for soil profile P3 at all locations, except at the structure's roof, which converged for $L/B > 8$. In contrast, soil profile P1 required larger domain sizes to minimize boundary effects through the use of periodic boundaries or DS at all locations, due to lower damping levels in dry soils.

Fig. 7e-g presents the foundation's normalized permanent settlement (δ/δ_{ILC}) and tilt (θ/θ_{ILC}) and the RMSE of excess pore pressures, Δu, at the $L/2$ location compared to ILC. For all indices, smaller domains in all containers led to notable effects on Δu, emphasizing the critical importance of domain size regardless of boundary type. For soil profile P3, smaller domains (i.e., $L/B \leq 2.7$ for the rigid container without DS and $L/B \leq 1$ with DS or for an FSB container with periodic lateral boundaries) reduced the predicted degree of soil softening, contributing to an underestimation of foundation settlements compared to ILC. Fig. 8 shows that the use of DS produced the most significant improvements at $L/B \leq 1$, resulting in a decrease in δ/δ_{ILC} compared to the case where DS was absent,

for all motions. In general, δ/δ_{ILC} converged to 1 for $L/B > 4$ for the FSB with periodic lateral boundaries, while a more extensive domain size was required ($L/B > 8$) for the rigid container with or without DS. Moreover, rapid convergence of settlement and tilt in dense, dry soil profile P1 is due to its low relative compressibility and high shear stiffness. In contrast, accelerations in P1 exhibited delayed converge influenced by lower damping, greater stiffness, motion mode interactions, and container boundary effects. Fig. 7f shows that θ/θ_{ILC} was strongly influenced by the domain size and container lateral boundary type. The restriction of deformation mechanisms within smaller containers promoted a stiffer response within the soil for these cases, which amplified θ/θ_{ILC}. Larger domains were therefore needed to allow for convergence of tilt (i.e., $L/B \geq 8$) for all boundary types considered.

3.2.3 Simulations of Soil-Structure-Container System with L/B = 2.7

3.2.3.1 Influence of Boundary Type on System Response

In this section, the influence of container type (rigid with DS versus rigid without DS or FSB box) on boundary effects within a container with $L/B = 2.7$ is evaluated in comparison with ILC in terms of shear strains, accelerations, excess pore water pressures, and settlement patterns. The container was designed at its maximum extent, considering the constraints of the centrifuge platform and structural dimensions. These comparisons aim to provide insights for comparing experimental and numerical results under inherent limitations of the experimental setup.

Shear strains

Fig. 9 compares the numerical predictions of contours of total shear strain at the end of shaking (ε_{xz}) for all soil profiles (P1-P3) and boundary types considered during motion M1. For the rigid container without DS (Fig. 9a) and all soil profiles, the development of shear deformations was interrupted by the stiff, rigid lateral boundaries of the container (as shown in Fig. 9a). The inclusion of DS allowed the shearing zone to propagate toward the container's edges, approaching the ILC in most cases. Overall, the FSB with periodic lateral boundaries (Fig. 9c) offered clear improvement in predicting shear strains compared to ILC, as expected. However, boundary effects were still observed due to the limited domain size. These trends were consistent without the presence of the structure during M1 and with a building during M2 and M3 (as shown in the supplementary materials, SM). The results indicate that the peak

ε_{xz} in cases without a building only represented 15% of ε_{xz} developed in similar models with a structure. As detailed in Table 4 and the SM, peak ε_{xz} within the soil domain was correlated with base motion intensity measures (IM), such as I_a and cumulative absolute velocity (CAV), with the largest peak ε_{xz} obtained during M2 followed by M3 and M1. This increase in seismic demand also increased boundary effects within the container. The performance of all boundary types, including FSB with periodic lateral boundaries, degraded for stronger motions, as evidenced by increased discrepancies between shear deformations in ILC and other containers with L/B = 2.7. The results also showed that the influence of boundary type on ε_{xz} was more noticeable in the vicinity of the lateral boundaries and appeared minor under the building at the center of the container. Note that the presence of DS also led to shear strain localization at the bottom of each lateral boundary due to the stiffness contrast between the two materials (particularly for soil profile P1).

Accelerations

Fig. 10 presents the average response spectra residuals (with respect to the ILC) for all motions as a function of boundary and soil profile type. The acceleration response was evaluated in the middle of the liquefiable layer for the saturated soil profiles and the middle of the dense layer for the dry soil profile (as identified in Fig. 4b) at a location farthest from the structure and container boundaries (i.e., $L/2$). This location was investigated to assess the ability of the soil-structure-container system to represent far-field conditions in the centrifuge. The residuals were defined by Eq. (2), where ILC replaced the reference case (SSC), and the second term referred to the different boundary types considered. All cases were examined with and without a structure in the center of the container.

In the case of a dry sand profile P1, the rigid lateral boundary conditions (Fig. 10a-b) underestimated the far-field spectral accelerations compared to ILC at short periods (with average residuals ranging from 0.1 to 1.1), both with and without a building. The benefit of DS inclusions was most evident in the dry condition (about 60% reduction over the period range of interest) compared to the saturated soils, because of lower inherent material damping. The average residuals in the saturated soil profiles P2-P3 in the rigid container were primarily negative at the depth shown in Fig. 4, indicating an overprediction of S_a compared to ILC. The difference between the S_a residuals in a rigid container

with and without DS was minor in soil profile P2, as the *L/2* readings at this depth overlaid zones of low shear strain both with and without a building due to a deeper formation of large deformations in this uniform soil profile (see Fig. 9 and the supplemental materials). In the layered, saturated soil profile P3, the *L/2* readings coincided with zones of moderate shear strain accumulation in models without a building or the edge of the building's zone in models with a building. In both saturated models, reductions in far-field S_a residuals with DS were up to about 45%, primarily in periods T = 0.1-0.9 s and T = 2.5-10 s. These trends were mostly consistent in the far-field at greater depths (z = 13 m) and under the building when compared to the same location in ILC, as shown in the SM. For soil profile P3, however, more visible improvements with DS were observed in far-field residuals at longer periods at z = 13 m (e.g., reductions of up to 60% at T > 2 s).

Periodic lateral boundaries (e.g., such as those in FSB) further reduced boundary effects within the container, with average residuals mostly centered around zero (Fig. 10). The minimum and maximum residuals (gray shaded area in the figures) were also considerably reduced compared to the rigid cases even with DS across the period range of interest. Including a structure in the container slightly increased the residuals in far-field accelerations for all soil profiles, due to soil-structure interaction (SSI), the greater shear strains within the soil domain (larger peak ε_{xz}), and the extension of the shearing zone toward the container's lateral boundaries (Fig. 9). The negative influence of including a structure in an FSB container was most evident at greater depths and longer periods for the saturated soil profiles P2-P3, increasing the residuals by up to about 150% compared to the case without a structure (see the SM). This is attributed to the combined effects of altered wave propagation patterns and lower damping within denser layers, SSI, and the inherent characteristics and flexibility of the FSB container.

Fig. 11 presents the RMSE of far-field spectral accelerations from T = 0.1-10 s as a function of depth (z) for the three soil profiles and boundary types and averaged for all motions. These results are presented at an *L/2* distance from the foundation's edge and container boundaries with a structure. Overall, for all soil profiles, periodic lateral boundaries led to the best performance (lowest RMSE) over most depths, followed by the rigid container with DS and then, the rigid container without DS. The largest difference between the far-field S_a RMSE of different boundary types was observed at

shallow depths in soil profile P1 while following zones of maximum shear strain in the saturated soil profiles (at greater depths in P2 and the bottom of the liquefiable layer in P3, Fig. 9). This is attributed to variations in shear strain concentrations within different soil profiles and boundary conditions. For the dry soil profile P1, the rigid boundaries with DS slightly reduced the error compared to periodic lateral boundaries.

Seismic performance indices

Fig. 12 provides comparisons of S_a RMSE at different locations within the container (i.e., at the center when without a structure, at *L/2* with a structure, on the foundation, and under the building) as a function of the soil profile type and the cumulative absolute velocity (*CAV*) of the motion at the depth and location of interest. *CAV* was selected preliminarily for this comparison, as it has previously been identified as an optimum IM predictor of liquefaction consequences on buildings (Kramer and Mitchell 2006; Karimi and Dashti 2017; Bullock et al. 2019b-c). In general, the use of DS slightly reduced the calculated S_a RMSE values, particularly for the case without a structure (Fig. 12a) and at the foundation level (Fig. 12d) for all the motions considered, confirming the trends previously observed in Fig. 9. The results demonstrated that boundary effects were soil profile-dependent, where, on average, the largest S_a RMSE in a rigid container was observed for the dry soil profile P1, and the smallest RMSE for soil profile P2 with the greatest material damping. Additionally, S_a RMSE increased with *CAV*, corresponding to increased cumulative seismic demand (in terms of amplitude and duration) within the container.

The influence of container boundaries on the seismic performance of the structure was subsequently evaluated by comparing the permanent foundation settlement (δ/δ_{ILC}) and tilt (θ/θ_{ILC}) normalized by the ILC's response in Fig. 13. The RMSE of far-field excess pore water pressures (Δu) obtained in the middle of the liquefiable layer at *L/2* for the saturated soil profiles P2-P3 was also compared in Fig. 13c. The computed δ/δ_{ILC} ratios were mostly centered around 1, suggesting a reasonable approximation of ILC and minor boundary effects in terms of this index. The normalized tilt was the most influenced by the use of a rigid container, particularly for the saturated soil profiles that experienced softening and liquefaction, with ratios diverging from 1 both with and without DS. While

the use of DS slightly increased the calculated RMSE Δu values, all boundary types successfully captured the magnitude and rate of excess pore water pressure generation compared to ILC (as shown in the SM). Boundary effects were primarily evident through overestimated dilation cycles and rapid drops in excess pore water pressure during shaking when using rigid boundaries (w/ & w/o DS). In general, FSB with periodic lateral boundaries was the most effective in reducing boundary effects, particularly in terms of θ/θ_{ILC}, with ratios closer to 1 for all soil profiles. Finally, no clear trends were observed in relation to ground motion characteristics, such as CAV, for δ/δ_{ILC} and θ/θ_{ILC}, while RMSE of Δu increased with CAV. This suggests that boundary effects on the foundation's movements did not depend as strongly on ground motion characteristics, compared to effects on accelerations and pore water pressures.

In general, the shear strain contours, accelerations, excess pore water pressures, and permanent settlement and tilt responses of the foundation were sensitive to the container type and use of DS. While an FSB container offered the best performance compared to an ILC, DS offered improvements in rigid containers in terms of accelerations and shear strains in the three soil profiles for L/B = 2.7. The influence of DS on accelerations and excess pore water pressures was shown to be sensitive to ground motion characteristics. Based on these observations, DS was included in the planned experiments within a transparent rigid container.

3.2.3.2 Selection of Duct Seal Geometry

To determine the appropriate DS thickness (w_{DS}) that reduces boundary effects on the performance measures or indices of interest within the rigid container, w_{DS} was varied numerically from 15 to 70 mm [1 to 5 m in prototype scale] (as shown in Fig. 14). The domain length (or container size) was kept constant in these simulations. The boundary effects for the three motions were averaged and presented for each soil profile with a structure within the rigid container. Overall, the results highlight that increasing w_{DS} is not always beneficial because the total boundary length was kept constant, reducing the available boundary length (L). The smaller w_{DS} of 1 m [in prototype units], in this case, led to the best predictions of spectral accelerations in soil profiles P1 and P2 (particularly near the building) when compared to ILC. The S_a RMSE gradually increased with increasing w_{DS}, reaching its peak at w_{DS} = 5

m. These results indicate that the benefits of a thicker DS did not outweigh the disadvantages of a reduced L within a fixed-size container, limiting the development of shear zones in the presence of a structure. Overall, the influence of w_{DS} was more visible in soil profile P1 with dry sand in terms of S_a indices, as expected due to smaller material damping. The RMSE differences among models with varying w_{DS} became minor in saturated soil profiles with increased damping, particularly for the liquefiable soil profile P3. These trends were consistent when comparing the S_a indices for different ground motions (shown in Fig. 15), where larger S_a RMSE values were obtained for greater w_{DS}. Fig. 15 also shows that the performance of DS degrades for larger amplitude motions (i.e., in terms of PGA), with S_a RMSE values reaching their peak during M3 (PGA = 0.83 g, CAV = 1,990 cm/s). Evaluating the structural performance indices in Figs. 14-15 shows that δ/δ_{ILC} was relatively insensitive to changes in w_{DS}, while θ/θ_{ILC} was highly sensitive to w_{DS} (i.e., or the domain size), although no clear trends were visible. This effect was more pronounced for the saturated soil profiles (Fig. 14) and M2 (Fig. 15). Finally, the results reveal a reduction in boundary effects in terms of Δu RMSE with thicker DS inclusions for stronger motions (i.e., M2 and M3 in terms of CAV, I_a, $D_{5\text{-}95}$), despite the reduction in model length.

Given the results obtained for soil profile P3 and M1 (which correspond to the baseline case for our intended centrifuge experiments) and considering that DS is typically commercially available in 1-inch thickness, a final thickness of 1 in (1.7 m in prototype scale) was selected to facilitate constructability, which was found to be consistent with other previous centrifuge PIV studies (e.g., Adamidis 2017). This thickness also led to reasonable simulations of accelerations, shear strains, foundation settlement, tilt, and excess pore water pressures at key locations in the soil profile of interest (e.g., soil profile P3).

4 IMAGE CAPTURE FOR DEFORMATION MEASUREMENT AND VISUALIZATION

In addition to a transparent window, the PIV system requires high frame rate cameras and high-resolution imaging capabilities, along with optimization of soil texture, powerful lighting, and precise synchronization of data acquisition. These components are necessary for the PIV system to measure

the effects of different soil deformation mechanisms. Fig. 16 provides a photograph of the new deformation measurement system at CU Boulder's centrifuge facility .

To maximize the precision of the image texture in PIV analysis, we followed the methodology described by Stanier and White (2013) to determine the appropriate amount of artificial seeding required for uniformly colored Ottawa F65 sand, a potential test soil. Their method for optimizing soil texture should be applied to test soils that constitute the predominant portion of the profile. In this case, a small rigid box with a plexiglass front face was used as a representative sample; for seeding calibration, we positioned this box at the intended location of the designed rigid container. The procedure was conducted for dry and saturated samples, maintaining the same exposure time. The required exposure time to avoid pixel/motion blur was estimated as 250 μs, based on the peak ground velocity recorded at the middle of the critical layer in the free-field from a previous centrifuge experiment. To differentiate between the dense and loose Ottawa layers, we selected two different colors for the artificial texture: blue for the dense layers and black for the loose layer. We used an oil-based dye to color the Ottawa sand, ensuring no bleeding during saturation. Gradually, the colored Ottawa sand was mixed evenly with uncolored sand and pluviated at Dr = 40% and 90%. For each of the colors, a representative range of the artificial seeding ratios (ASRs) observed in the procedure is presented in Fig. 17, along with other image texture quality metrics (see Appendix C for recommended thresholds) for the chosen optimally seeded sand (representing an ASR of 0.67 and 0.6 for the dense and loose Ottawa layers, respectively). Following Stanier and White (2013), the optimum PIV tracking precision occurs when the standard deviation of pixel intensities is the greatest. Therefore, we selected the percentages of artificial texture to be added in the potential experiments as 40% and 60% respectively for the loose and dense layers (Fig. 18). As expected, the range of mean standard deviation of pixel intensities was greater for the black dyed sand due to the additional contrast against the Ottawa sand. These results indicate that any uniformly colored test soil should be dyed with a distinct color to distinguish it from other layers during PIV analysis or excavation.

The application of centrifuge scaling laws for dynamic analysis necessitates reducing the duration of prototype scale motions by a factor of N (in our case, N = 70). Consequently, a high-speed camera was required in order to capture the images within this short (scaled) timeframe. For this purpose,

we selected a camera with a maximum resolution of 1440x1024 pixels (~1.5 MP) and a sampling rate of 2000 frames per second (fps) (Fig. 19a). In addition to the pixels and sampling rate, we selected the camera based on its high impact resistance, rated vibration resistance, and flexibility in memory recording. The chosen camera features a global shutter speed capture mode that enables the independent control of each pixel's exposure time, while simultaneously capturing the changes in all pixels. Table 5 compares the selected camera with those used in previous geotechnical image analyses studies. To achieve higher resolution while maintaining our desired field of view (FOV), we coupled the camera with a Kowa C-mount 16 mm fixed focal length lens with a minimum focus distance of 300 mm achieving a 0.24 mm/pixel ratio.

To maximize the observation area and cover the entire exposed plane of the soil model, we positioned one GoPro HERO 8 (GoPro Inc., USA) camera on each side of the high-speed camera. Given the high cost of high-speed cameras, these two GoPros provide a cost-effective alternative for PIV analysis. By combining the analysis results from each camera, we can achieve a full view of the deformation mechanism. The high-speed camera, placed at the center of the shake table, captures the response in the vicinity of the building, while the GoPros captured the far-field response and any boundary effects. However, lens modifications were required for the GoPros to match the high-speed camera's mm/pixel ratio, due to the GoPro's minimum focus distance of 305 mm and a mm/pixel ratio of 0.33. The modification choices for the two GoPros were strategically made to address specific needs. The first GoPro was modified with a 52 mm +4 macros lens, providing an affordable and accessible option, while allowing for sharply focused images with the desired mm/pixel ratio at distances shorter than the minimum focus distance (Fig. 19b). As the lens had a wide field of view setting, fisheye distortion correction were needed during image processing prior to analysis. The second GoPro was modified with a 2.7 mm 16MP low distortion M12 lens from Back-Bone Gear Inc. (Fig. 19c). This lens is well-suited for wide-angle shooting and reduces the minimum focus distance, while maintaining linear optics with no fisheye distortion, eliminating the need for post-processing adjustments. The lights will be activated with the start of the motion to synchronize the time between the two GoPros and the high-speed cameras. This synchronization allows to identify the frame precisely when the lights are turned back on during the post-processing stage. Additional details on the cameras, mounting system,

lights, and the computational procedure for the deformation measurement system are provided in the SM.

5 POTENTIAL APPLICATIONS OF THE DESIGNED EXPERIMENTAL SETUP

Our experimental setup and deformation measurement system enables systematic quantification and visualization of individual displacement mechanisms with or without a structural model on a mat foundation. The system is adaptable for a wide range of applications in which PIV holds promise for evaluating deformations within stratified, intermediate, or cohesive soils with a range of saturation degrees, underlying a variety of structures, foundation types, embankments, buried structures, and potential ground improvement techniques. In Fig. 20, we present a few examples intended to illustrate potential theoretical applications of the system.

Changing the dimensions of the superstructure or including additional adjacent underground or aboveground structures (e.g., to study seismic structure-soil-structure interaction) are expected to alter the required container length and/or duct seal thickness that minimize boundary effects. Further, Bessette et al. (2022) showed that the presence of an adjacent structure can significantly impact a building's permanent rotation, even when the separation distance exceeds 3.5 times its foundation width. Hence, for evaluating the response of isolated buildings or undergrounds structures within the selected container dimensions, we recommend placing only one structure in the center of the box.

When physically modeling the response of layered, liquefiable deposits, it is critical to replicate the surface manifestation of ejecta, as typically observed in the field. The potential for ejecta is known to be influenced by stratigraphic variability, as well as the depth to the groundwater table. To explore the ejecta phenomena, we recommend using a series of realistic, liquefiable soil deposits. The example soil profiles shown in Fig. 20a base these realistic soil deposits on case history observations from the Canterbury earthquake sequence in Christchurch where ejecta was observed (Hutabarat & Bray 2021). We also carefully considered the groundwater table depth for this example, using one-dimensional (1D) single column analyses to determine the groundwater table depth required to generate surface ejecta. This calculation was based on the ejecta potential index (EPI) and severity classifications introduced by Hutabarat and Bray (2021), which were shown to correlate well with the Christchurch case history

database. The water table was varied to determine the minimum depth necessary to reach an ejecta classification of "severe" within the soil profiles of interest. We also considered the volume of water pushed into the air and the water surface curvature resulting from the centrifugal force, to keep the water table above the critical layer at all locations within the centrifuge container. The analyses showed that a minimum groundwater table depth of 0.9 m [prototype scale] is required for the formation of surface ejecta.

Ground improvement techniques can also be modeled with the developed container-PIV system, and their impact on individual mechanisms of deformation evaluated and visualized. For example, dense granular columns (DGCs), which combine mitigation mechanisms associated with drainage, shear reinforcement, and installation-induced densification, can be designed, constructed, and placed across the width of the container, with a half-cylindrical configuration at the plexiglass interface based on symmetry and plane strain conditions. Previous case histories and experimental studies have demonstrated the potential of DGCs as an effective mitigation solution, with significant reductions in permanent foundation settlement and in the amplitude or duration of large excess pore water pressures (Adalier et al. 2003, 2004; Badanagki et al. 2018, 2019; Tiznado et al. 2020).

Fig. 20b shows an example application of the designed granular column configuration with the new container and deformation measurement system. The DGCs, in this example, were positioned at a set spacing to span the entire width of the box, to simulate plane-strain conditions. Previous case histories and centrifuge experiments have demonstrated the effectiveness of DGCs in mitigating liquefaction consequences, even with area replacement ratios (Ar) as low as 10% (Hausler 2002; Nikolaou et al. 2016; Tiznado et al. 2020), where Ar represents the ratio of DGC area to the tributary area of the granular column (Baez and Martin 1993). Therefore, this Ar ratio was selected for the specific experimental setup shown in Fig. 20b due to its practicality, facilitating easier model construction. The researcher may select a different Ar, while considering practical implications of a denser DGC configuration and challenges associated with construction and proximity to sensors.

Additional design considerations for the width and depth of ground improvement beyond the dimensions of the structure are provided by JGS (1998). In this example, we constructed the DGCs with closed-end geotextile cylinders to avoid clogging in subsequent shaking. The cylinders can then be

filled with granular soils (typically fine gravel) and compacted in layers of 1 cm in thickness to achieve a final relative density (*Dr*) exceeding about 85% based on calibration trials (Tiznado et al. 2020). The columns should be vertically positioned in the container before the soil layers are pluviated, unless an automated system is available to install columns in flight. This preparation method, along with the use of geotextile filters, serves multiple purposes: it (1) facilitates model construction and repeatability, (2) prevents clogging caused by the transportation of fines from the surrounding soil during consecutive shaking, thus preserving their drainage capacity, and (3) avoids localized densification during column installation.

The first row of DGCs at the interface with the container plexiglass should be constructed as half-columns (representing a symmetric state into the page). This is to allow for visualization of deformation mechanisms around the DGCs through the transparent container, as illustrated in Fig. 20c. Anticipating the limitations of the experimental setup, certain approximations will be required. For example, within the geotextile mold, a thin acrylic sheet with a thickness of 1 mm can be placed on the flat side of the half-column (in contact with the Perspex window). This addition can help prevent bulging from the compaction of granular soils within the geotextile mold. During model preparation, a water-soluble tape can be employed to secure the columns against the window. Additionally, a layer of liquid latex can be applied to seal the interface between the acrylic piece and the window to prevent potential infiltration of water or sand particles at the interface. The selection of liquid latex is based on its flexibility and ability to move with the soil without providing additional reinforcement, which was confirmed through several calibration trials. This set up presents one possible configuration for ground improvement, which can guide the design considerations for other conditions and types of ground improvement in the future.

6 CONCLUSIONS

This paper describes the design, construction, and approximations involved in developing a new deformation measurement and visualization system for centrifuge modeling of liquefiable deposits. The development of this system aims to reliably model, measure, and visualize various deformation mechanisms contributing to total surface deformations. In this paper, we provide a detailed overview

of the design aspects of each of the system's components, including a linear elastic SDOF structure, a transparent rigid centrifuge container, duct seal inclusions, PIV system, camera requirements and measurements, and highlight general example applications of the system.

In this study, we use fully-coupled, 3-D nonlinear finite element analyses to examine the influence of domain size and container type on boundary effects within different soil-structure-container systems and guide the design of the duct seal geometry and soil/groundwater conditions. The findings highlight the critical importance of considering the proximity of key measurements to lateral boundaries in any centrifuge container type in order to minimize wave reflection effects on accelerations, foundation settlement, tilt, excess pore pressures, and shear strains. As expected, the parametric study shows that periodic lateral boundaries can be highly effective in reducing boundary effects in liquefiable soils. Notably, settlement of a foundation-structure placed at the center of the container exhibited convergence with periodic boundaries at a normalized distance to lateral boundaries (L/B) > 4. In contrast, rigid containers, both with and without duct seal (DS), present practical challenges, necessitating larger domains for convergence of settlement values (L/B > 8). Nevertheless, the results show the value of incorporating DS on the sidewalls of rigid boxes in smaller container sizes with L/B < 1 that are commonly employed in PIV studies. DS proves particularly beneficial in improving the accuracy of predicted settlements under these conditions. In addition, the results indicate that larger domains ($L/B \geq 8$) are essential for achieving convergence of foundation tilt across all boundary types. The benefits of a thicker DS often do not outweigh the disadvantages of a reduced L within a fixed-size container in terms of accelerations. This limitation imposes constraints on developing shear zones below structures, emphasizing knowledge of the trade-offs in container design for accurate experimental outcomes. Though not fully generalizable, this paper's observations and results are intended to guide the design process for the next generation of dynamic centrifuge experiments investigating soil-structure interaction and visualizing displacement mechanisms within more realistic, interlayered, and stratigraphically variable soil deposits.

7 AUTHOR STATEMENT

Caroline Bessette: Investigation, Data curation, Formal analysis, Conceptualization, Methodology, Writing-Original draft

Lianne Brito: Investigation, Data curation, Formal analysis, Conceptualization, Methodology, Writing-Original draft

Shideh Dashti: Conceptualization, Methodology, Funding acquisition, Writing, Reviewing & Editing.

Abbie Liel: Conceptualization, Methodology, Funding acquisition, Writing, Reviewing & Editing.

Brad Wham: Conceptualization, Methodology, Funding acquisition, Writing, Reviewing & Editing.

8 DECLARATION OF COMPETING INTERESTS

The authors declare that they have no known competing financial interests or personal relationships that could have appeared to influence the work reported in this paper.

9 DATA AVAILABILITY

Data will be made available upon request.

10 ACKNOWLEDGEMENTS

This work was supported by the National Science Foundation (NSF) under grant no. 2135669, the Natural Sciences and Engineering Research Council of Canada (NSERC), the Graduate Assistance in Areas of National Need (GAANN), and the NSF Graduate Research Fellowship (GRFP). This work utilized the Alpine high-performance computing resource at the University of Colorado Boulder. Alpine is jointly funded by the University of Colorado Boulder, the University of Colorado Anschutz, Colorado State University, and the National Science Foundation (award 2201538). The results presented in this paper reflect the opinions of the authors only and do not reflect the viewpoint of any of the funding agencies.

11 REFERENCES

Adalier K, Elgamal A. Mitigation of liquefaction and associated ground deformations by stone columns. Engineering Geology. 2004;72(3-4):275–291. https://doi.org/10.1016/j.enggeo.2003.11.001.

Adalier K, Elgamal A, Meneses J, Baez JI. Granular columns as liquefaction counter-measure in non-plastic silty soils. Soil Dyn Earthquake Eng. 2003;23(7):571–584. https://doi.org/10.1016/S0267-7261(03)00070-8.

Adamidis O, Madabhushi SPG. Rocking response of structures with shallow foundations on thin liquefiable layers. Géotechnique. 2022;72(2):127-145.

Adamidis O, Madabhushi SPG. Deformation mechanisms under shallow foundations on liquefiable layers of varying thickness. Géotechnique. 2018;68(7):602-613.

Adamidis O. Earthquake-Induced Liquefaction of Sand and Response of Structures with Shallow Foundations [PhD Dissertation]. University of Cambridge; 2017.

American Society of Civil Engineers. Minimum design loads for buildings and other structures. 2013.

Badanagki M, Dashti S, Paramasivam B, Tiznado JC. How Do Granular Columns Affect the Seismic Performance of Non-Uniform Liquefiable Sites and Their Overlying Structures? Soil Dynamics and Earthquake Engineering. 2019;125:105715. https://doi.org/10.1016/j.soildyn.2019.105715.

Badanagki M, Dashti S, Kirkwood P. Influence of Dense Granular Columns on the Performance of Level and Gently Sloping Liquefiable Sites. Journal of Geotechnical and Geoenvironmental Engineering. 2018;144(9):04018065. https://doi.org/10.1061/(ASCE)GT.1943-5606.0001937.

Bardet JP, Huang Q, Chi SW. Numerical prediction for model no 1. In: Arulanandan K, Scott RF, editors. Proc., Int. Conf. on the Verification of Numerical Procedures for the Analysis of Soil Liquefaction Problems. Rotterdam, Netherlands: A.A. Balkema; 1993. p. 67–86.

Beyzaei CZ, et al. Depositional environment effects on observed liquefaction performance in silt swamps during the Canterbury earthquake sequence. Soil Dynamics and Earthquake Engineering. 2018a;107:303-321.

Beyzaei CZ, et al. Laboratory-based characterization of shallow silty soils in southwest Christchurch. Soil Dynamics and Earthquake Engineering. 2018b;110:93-109.

Bhattacharya S, Lombardi D, Dihoru L, Dietz MS, Crewe AJ, Taylor CA. Model container design for soil-structure interaction studies. InRole of seismic testing facilities in performance-based earthquake engineering: SERIES workshop 2012 (pp. 135-158). Springer Netherlands.

Brennan AJ, Madabhushi SP. Design and performance of a new deep model container for dynamic centrifuge testing. In Physical Modelling in Geotechnics 2022 Nov 22 (pp. 183-188). Routledge.

Bullock Z, Karimi Z, Dashti S, Porter K, Liel AB, Franke KW. A physics-informed semi-empirical probabilistic model for the settlement of shallow-founded structures on liquefiable ground. Géotechnique. 2019a;69(5):406–19. https://doi.org/10.1680/jgeot.17.P.174.

Bullock Z, Dashti S, Karimi Z, Liel A, Porter K, Franke K. Probabilistic models for residual and peak transient tilt of mat-founded structures on liquefiable soils. Journal of Geotechnical and Geoenvironmental Engineering. 2019b;145(2):04018108. https://doi.org/10.1061/(ASCE)GT.1943-5606.0002002.

Bullock Z, Dashti S, Liel AB, Porter KA, Karimi Z. Assessment supporting the use of outcropping rock evolutionary intensity measures for prediction of liquefaction consequences. Earthquake Spectra. 2019c;35(4):1899–1926. https://doi.org/10.1193/041618EQS094M.

Chakrabortty P, Popescu R. Numerical Simulation of Centrifuge Tests on Homogeneous and Heterogeneous Soil Models. Computers and Geotechnics. 2012;41:95–105. https://doi.org/10.1016/j.compgeo.2011.11.008.

Cheney JA, Hor OY, Brown RK, Dhat NR. Foundation vibration in centrifuge models. In Proc. Centrifuge 1988 (Vol. 88, pp. 481-486).

Cilingir U, Madabhushi SPG. A Model Study on the Effects of Input Motion on the Seismic Behaviour of Tunnels. Soil Dynamics and Earthquake Engineering. 2011;31(3):452–462. https://doi.org/10.1016/j.soildyn.2010.10.004.

Cilingir U, Madabhushi SP. Particle image velocimetry analysis in dynamic centrifuge tests. InProceedings of the 7th International Conference on Physical Modelling in Geotechnics (ICPMG) 2010 Jun 17 (pp. 319-324). Zurich: CRC Press.

Cubrinovski M, et al. Liquefaction effects and associated damages observed at the Wellington CentrePort from the 2016 Kaikoura earthquake. Bulletin of the New Zealand Society for Earthquake Engineering. 2017;50(2):152-173.

Das BM, Sobhan K. Principles of geotechnical engineering. Cengage Learning, Boston, Massachusetts; 2016.

Dashti S, Bray JD, Pestana JM, Riemer M, Wilson D. Mechanisms of seismically induced settlement of buildings with shallow foundations on liquefiable soil. Journal of geotechnical and geoenvironmental engineering. 2010a Jan;136(1):151-64.

Dashti S, Bray JD, Pestana JM, Riemer M, Wilson D. Centrifuge testing to evaluate and mitigate liquefaction-induced building settlement mechanisms. Journal of geotechnical and geoenvironmental engineering. 2010b Jul;136(7):918-29.

Elgamal A, Yang Z, Parra E. Computational modeling of cyclic mobility and post liquefaction site response. Soil Dynamics and Earthquake Engineering. 2002;22(4):259–271. https://doi.org/10.1016/S0267-7261(02)00022-2.

Fema A. 440, Improvement of nonlinear static seismic analysis procedures. FEMA-440, Redwood City. 2005;7(9):11.

Goel RK, Chopra AK. Period formulas for moment-resisting frame buildings. Journal of Structural Engineering. 1997 Nov;123(11):1454-61.

Heron CM. The dynamic soil structure interaction of shallow foundations on dry sand beds [PhD Dissertation]. University of Cambridge; 2013.

Hutabarat D, Bray JD. Seismic response characteristics of liquefiable sites with and without sediment ejecta manifestation. Journal of Geotechnical and Geoenvironmental Engineering. 2021 Jun 1;147(6):04021040.

Hwang YW, Dashti S, Kirkwood P. Impact of ground densification on the response of urban liquefiable sites and structures. Journal of Geotechnical and Geoenvironmental Engineering. 2022;148:1–04021175.

Hwang YW, Ramirez J, Dashti S, Kirkwood P, Liel AB, Camata G, Petracca M. Seismic Interaction of Adjacent Structures on Liquefiable Soils: Insight from Centrifuge and Numerical Modeling. ASCE Journal of Geotechnical and Geoenvironmental Engineering. 2021;147(8):04021063.

Hwang YW. Numerical Modeling of Structure-Soil-Structure Interaction on Liquefiable Soils and Effects of Mitigation in Urban Settings. [PhD Dissertation] University of Colorado Boulder; 2020.

Karimi Z, Dashti S. Ground Motion Intensity Measures to Evaluate II: The Performance of Shallow-Founded Structures on Liquefiable Ground. Earthquake Spectra. 2017;33(1):277–298. https://doi.org/10.1193/103015EQS163M.

Karimi Z, Dashti S. Numerical and Centrifuge Modeling of Seismic Soil–Foundation–Structure Interaction on Liquefiable Ground. Journal of Geotechnical and Geoenvironmental Engineering. 2016a;142(1):04015061. https://doi.org/10.1061/(ASCE)GT.1943-5606.0001346.

Karimi Z, Dashti S. Seismic Performance of Shallow Founded Structures on Liquefiable Ground: Validation of Numerical Simulations Using Centrifuge Experiments. Journal of Geotechnical and Geoenvironmental Engineering. 2016b;142(6):04016011. https://doi.org/10.1061/(ASCE)GT.1943-5606.0001479.

Kassas K, Adamidis O, Anastasopoulos I. Shallow Strip Foundations Subjected to Earthquake-Induced Soil Liquefaction: Validation, Modelling Uncertainties, and Boundary Effects. Soil Dynamics and Earthquake Engineering. 2021;147:106719. https://doi.org/10.1016/j.soildyn.2021.106719.

Kokusho T, Fujita K. Water films involved in post-liquefaction flow failure in Niigata City during the 1964 Niigata earthquake. 2001.

Kramer SL, Mitchell RA. Ground Motion Intensity Measures for Liquefaction Hazard Evaluation. Earthquake Spectra. 2006;22(2):413–438. https://doi.org/10.1193/1.2194970.

Kwok AOL, Stewart JP, Hashash YMA, Matasovic N, Pyke R, Wang Z, Yang Z. Use of exact solutions of wave propagation problems to guide implementation of nonlinear seismic ground response analysis procedures. J. Geotech. Eng. 2007;133(11):1385–1398.

Luque R, Bray JD. Dynamic analyses of two buildings founded on liquefiable soils during the Canterbury earthquake sequence. Journal of Geotechnical and Geoenvironmental Engineering. 2017;143(9):04017067.

Maharjan M, Takahashi A. Centrifuge model tests on liquefaction-induced settlement and pore water migration in non-homogeneous soil deposits. Soil Dynamics and Earthquake Engineering. 2013;55:161-169.

Malvick EJ, Kutter BL, Boulanger RW, Kulasingam R. Shear localization due to liquefaction-induced void redistribution in a layered infinite slope. Journal of Geotechnical and Geoenvironmental Engineering. 2006 Oct;132(10):1293-303.

Mazzoni S, McKenna F, Scott M, Fenves G. Open system for earthquake engineering simulation user command-language. Berkeley, CA: Network for Earthquake Engineering Simulations; 2006.

Menq FY. Seismic soil-pile-structure interaction: experiments, theory and practice. Soil Dynamics and Earthquake Engineering. 2003;23(8):635-649.

Nikolaou S, Vera-Grunauer X, Gilsanz R. GEER-ATC earthquake reconnaissance, April 16, 2016, Muisne, Ecuador. Rep. No. GEER-049. Geotechnical Extreme Events Reconnaissance Association; 2016.

Olarte J, Paramasivam B, Dashti S, Liel A, Zannin J. Centrifuge modeling of mitigation-soil-foundation-structure interaction on liquefiable ground. Soil Dynamics and Earthquake Engineering. 2017;97:304–323. https://doi.org/10.1016/j.soildyn.2017.03.014.

Orang MJ, Boushehri R, Motamed R, Prabhakaran A, Elgamal A. An Experimental Evaluation of Helical Piles as a Liquefaction-Induced Building Settlement Mitigation Measure. Soil Dynamics and Earthquake Engineering. 2021;151:106994. https://doi.org/10.1016/j.soildyn.2021.106994.

Olarte J, Dashti S, Liel AB. Can ground densification improve seismic performance of the soil-foundation-structure system on liquefiable soils? Earthquake Engineering & Structural Dynamics. 2018 Apr 25;47(5):1193-211.

Pak RYS, Soudkhah M, Abedzadeh F. Experimental Synthesis of Seismic Horizontal Free-Field Motion of Soil in Finite-Domain Simulations with Absorbing Boundary. Soil Dynamics and Earthquake Engineering. 2011;31(11):1529–1539. https://doi.org/10.1016/j.soildyn.2011.06.002.

Pak RY, Guzina BB. Dynamic characterization of vertically loaded foundations on granular soils. Journal of geotechnical engineering. 1995 Mar;121(3):274-86.

Paramasivam B. Influence of Traditional and Innovative Liquefaction Mitigation Strategies on the Performanc of Soil-structure Systems, Considering Soil Heterogeneity [PhD Dissertation]. University of Colorado at Boulder; 2018.

Paramasivam B, Dashti S, Liel A. Impact of Spatial Variations in Permeability of Liquefiable Deposits on Seismic Performance of Structures and Effectiveness of Drains. Journal of Geotechnical and

Geoenvironmental Engineering. 2019;145(8):04019030. https://doi.org/10.1061/(ASCE)GT.1943-5606.0002054.

Paramasivam B, Dashti S, Liel A. Influence of Prefabricated Vertical Drains on the Seismic Performance of Structures Founded on Liquefiable Soils. Journal of Geotechnical and Geoenvironmental Engineering. 2018;144(10):04018070. https://doi.org/10.1061/(ASCE)GT.1943-5606.0001950.

Popescu R, Prevost JH. Centrifuge Validation of a Numerical Model for Dynamic Soil Liquefaction. Soil Dynamics and Earthquake Engineering. 1993;12:73–90. https://doi.org/10.1016/0267-7261(93)90047-U.

Port and Harbour Research Institute (PHRI). Handbook on Liquefaction Remediation of Reclaimed Land. A.A. Balkema, Rotterdam, The Netherlands; 1997.

Ramirez J. Numerical modeling of the influence of different liquefaction remediation strategies on the performance of potentially inelastic structures. Ph.D. dissertation, Dept. of Civil, Environmental and Architectural Engineering, Univ. of Colorado Boulder; 2019.

Ramirez J, Barrero AR, Chen L, Dashti S, Ghofrani A, Taiebat M, Arduino P. Site Response in a Layered Liquefiable Deposit: Evaluation of Different Numerical Tools and Methodologies with Centrifuge Experimental Results. Journal of Geotechnical and Geoenvironmental Engineering. 2018;144(10):04018073. https://doi.org/10.1061/(ASCE)GT.1943-5606.0001947.

Sancio R, Bray JD, Durgunoglu T, Onalp A. Performance of buildings over liquefiable ground in Adapazari, Turkey. InProc., 13th World Conf. on Earthquake Engineering 2004 Aug 1. Vancouver, Canada: Canadian Association for Earthquake Engineering.

Seed HB, Idriss IM. Soil moduli and damping factors for dynamic response analyses. Technical Report NCEER-97-0022, National Center for Earthquake Engineering Research; 1970.

Stanier S, White D. Improved image-based deformation measurement in the centrifuge environment. Geotechnical Testing Journal. 2013 Sep 17;36(6):915-28.

Steedman RS, Madabhushi SP. Wave propagation in sands. InProceedings of the international conference on seismic zonation, Stanford University, California 1991.

Tiznado JC, Dashti S, Ledezma C, Wham BP, Badanagki M. Performance of Embankments on Liquefiable Soils Improved with Dense Granular Columns: Observations from Case Histories and Centrifuge Experiments. Journal of Geotechnical and Geoenvironmental Engineering. 2020;146(9):04020073. https://doi.org/10.1061/(ASCE)GT.1943-5606.0002309.

Whitman RV, Lambe PC. Effect of boundary conditions upon centrifuge experiments using ground motion simulation. Geotechnical Testing Journal. 1986 Jun 1;9(2):61-71.

Yang Z, Lu J, Elgamal A. OpenSees soil models and solid fluid fully coupled elements: User's manual. San Diego: Dept. of Structural Engineering, Univ. of California; 2008.

Yang Z, Elgamal A. Numerical modeling of earthquake site response including dilation and liquefaction. Structural Systems Research Project Rep. No. SSRP-2000/01. San Diego: Dept. of Structural Engineering, Univ. of California; 2000.

Zienkiewicz OC, Chan AH, Pastor M, Paul DK, Shiomi T. Static and dynamic behaviour of soils: a rational approach to quantitative solutions. I. Fully saturated problems. Proceedings of the Royal Society of London. A. Mathematical and Physical Sciences. 1990;429(1877):285-309.

Zupan, J. D. Seismic performance of buildings subjected to soil liquefaction [PhD Dissertation]. University of California, Berkeley; 2014.

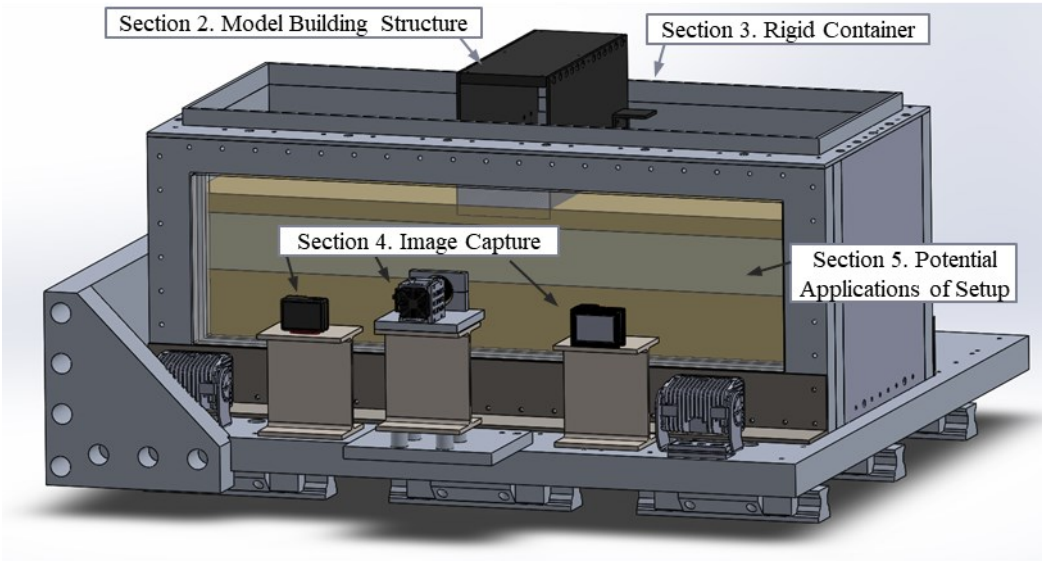

Figure 1. Schematic of different components outlined in this paper of dynamic centrifuge models for measurement and visualization of deformation mechanisms.

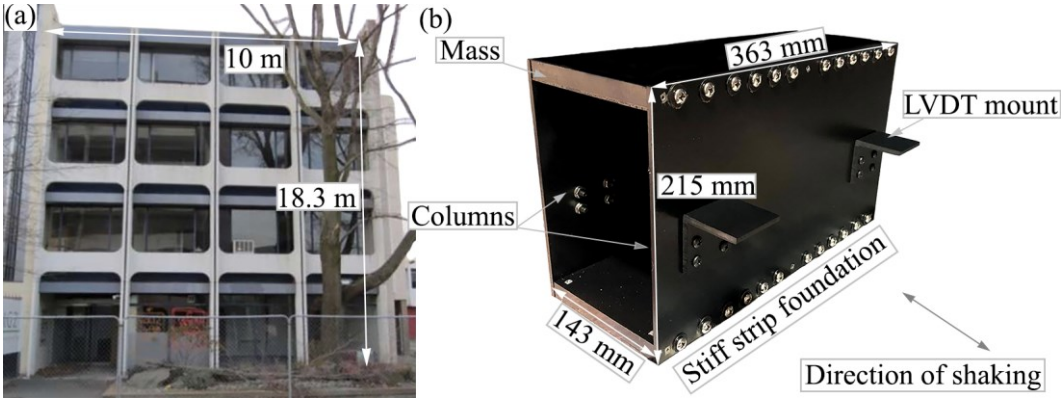

Figure 2. (a) Modified target building with dimensions in prototype scale, (b) model SDOF structure used in the centrifuge with dimensions in model scale.

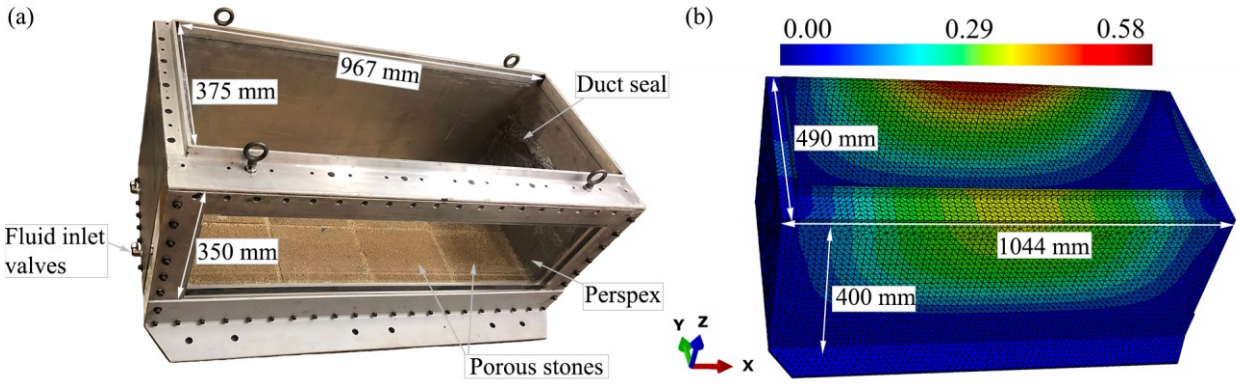

Figure 3. The rigid box container designed for the centrifuge experiments: (a) photograph of the fabricated container and the inside dimensions in model scale, (b) results of static estimation of lateral displacements in Abaqus, used in design (deformation in mm and the outside container dimensions in model scale).

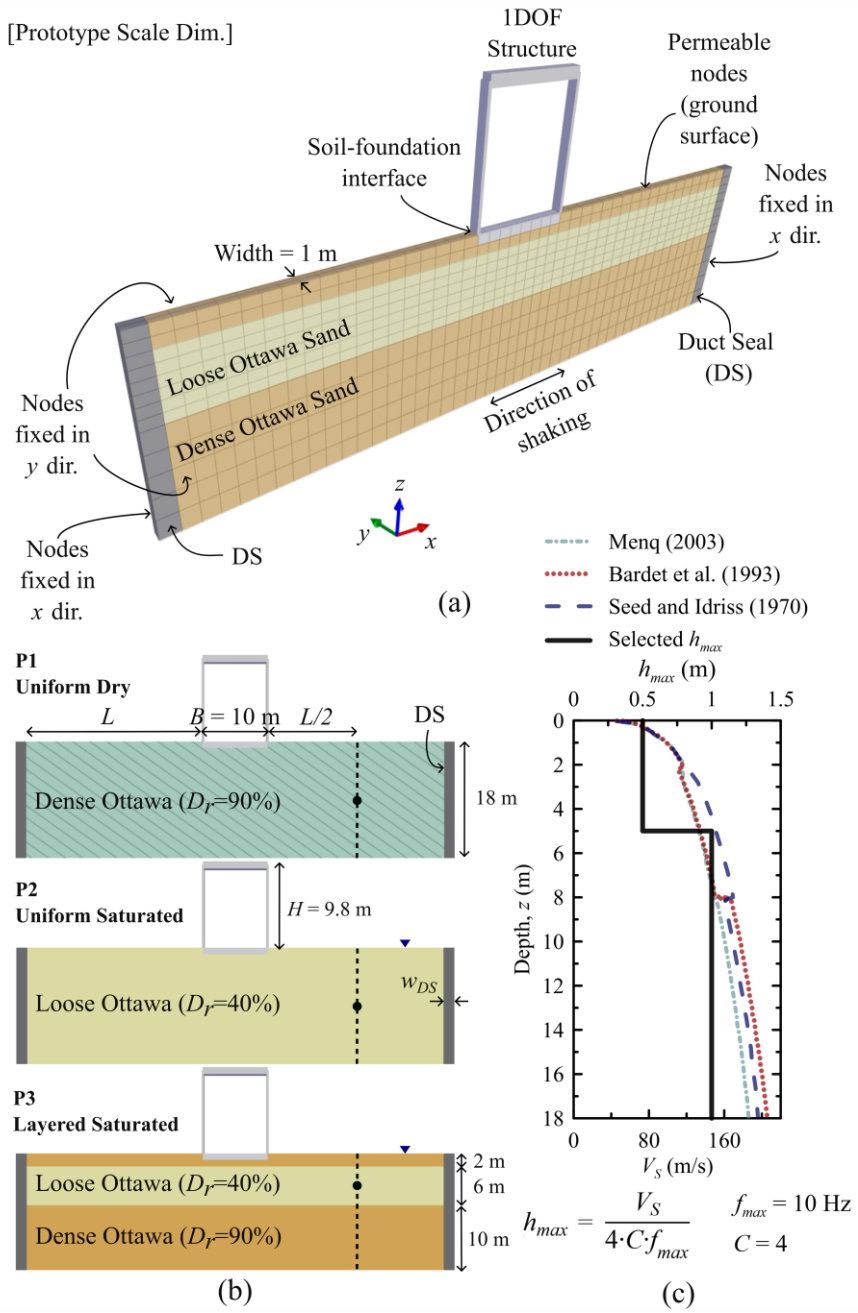

Figure 4. (a) Schematic view of the 3D model of soil profile P3 with the assigned boundary conditions (all units are in prototype scale meters); (b) Details of soil profile configurations; (c) Shear wave velocity profile [using empirical procedures from Seed and Idriss (1970), Bardet et al. (1993), and Menq (2003)] and selection of element size distribution for soil profile P3.

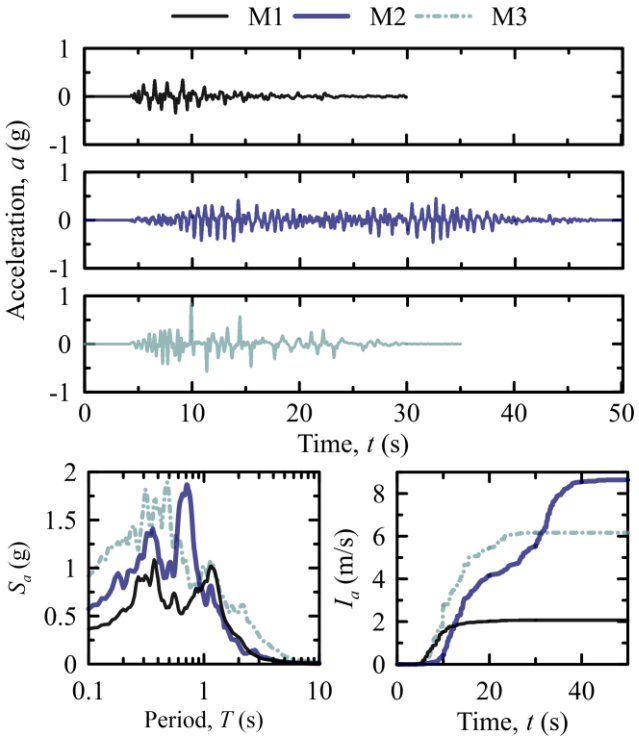

Figure 5. Acceleration and Arias Intensity (I_a) time histories and response spectrum (5%-damped) of the earthquake motions (M1-M3) used as input motion in the numerical analyses.

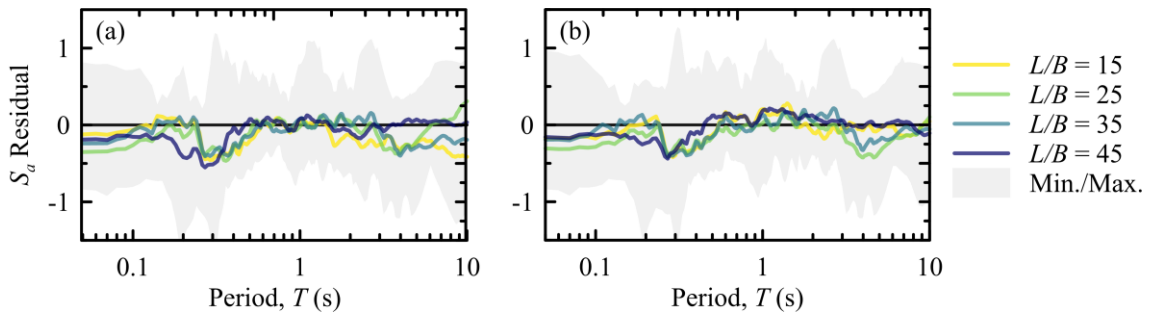

Figure 6. Comparison of the average S_a residuals for L/B = 15, 25, 35, 45 in soil profiles P1-3 during motions M1-3 as compared to a single free-field column in the middle of the liquefiable layer (or middle of the dense layer for soil profile P1) to determine the domain size for the Idealized Laminar Container: a) without a building in the center of the container; and b) with a building at an $L/2$ distance from the foundation edge. The gray shaded area outlines the minimum and maximum responses obtained from all analyses.

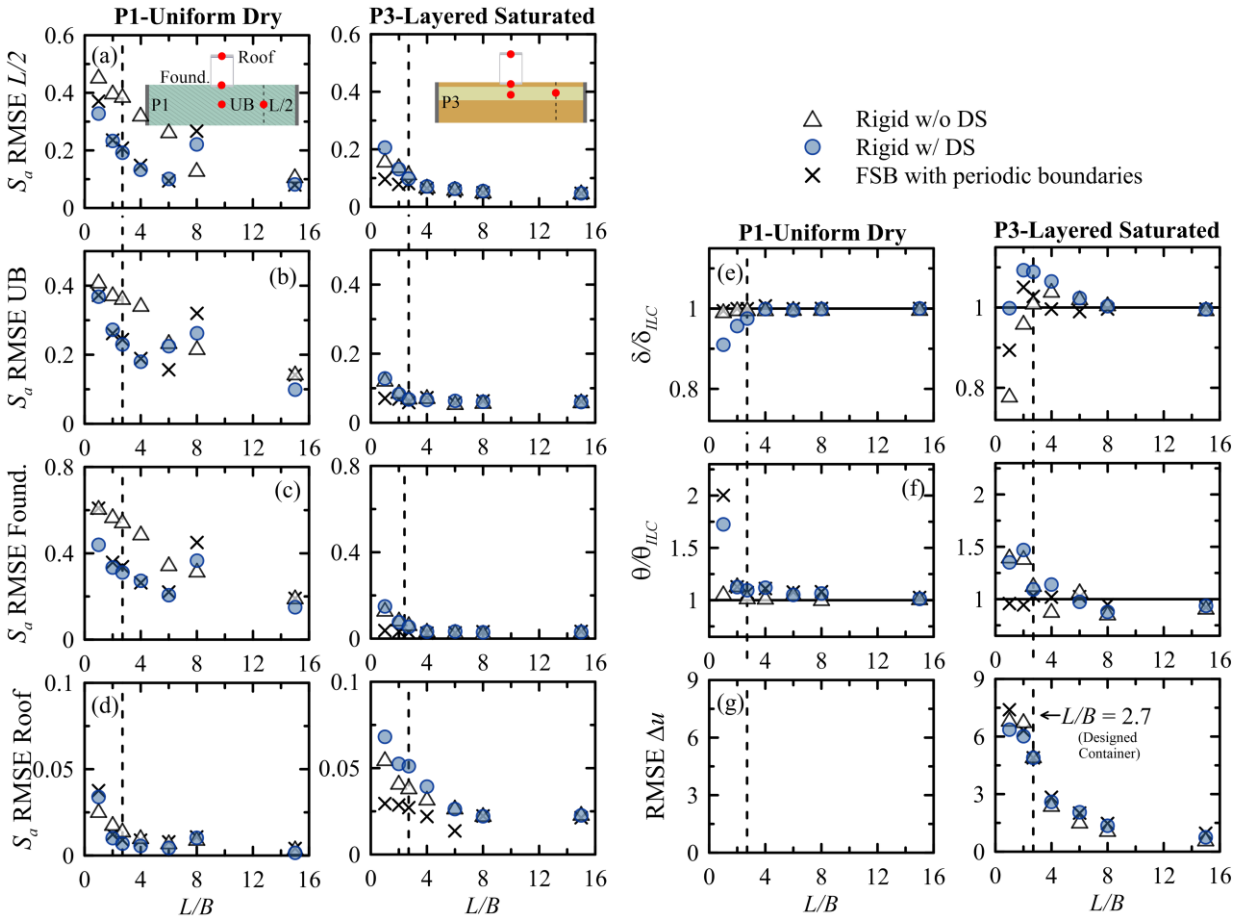

Figure 7. Comparison of the influence of the distance to the lateral boundaries (L/B) and boundary type for soil profiles P1 and P3 on the seismic performance indices averaged for the three motions, including the RMSE of spectral accelerations from T = 0.1-10 s at: a) $L/2$ and b) under the building (UB) in the middle of the liquefiable layer (or middle of the dense layer for soil profile P1); c) on the foundation and d) on the roof; e) normalized permanent foundation settlement (δ/δ_{ILC}); f) permanent foundation tilt (θ/θ_{ILC}), and g) RMSE of excess pore water pressure (Δu) in the middle of the liquefiable layer.

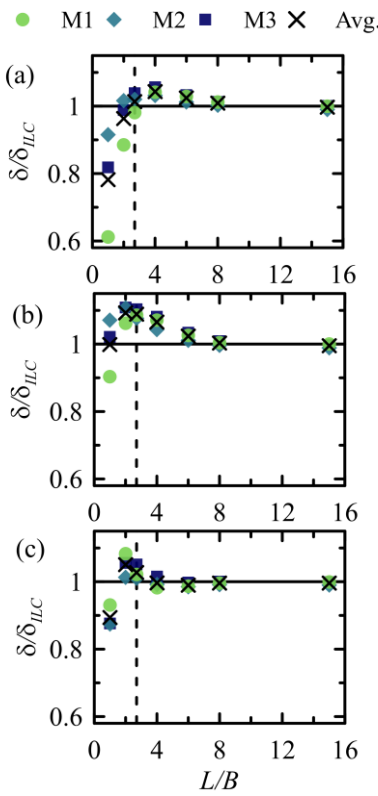

Figure 8. Comparison of the influence of the distance to the lateral boundaries (L/B) and ground motion (M1-M3) on the permanent foundation settlement relative to the ILC (δ/δ_{ILC}) for soil profile P3 and the following containers: a) rigid without DS; b) rigid with DS; and c) FSB with periodic boundaries.

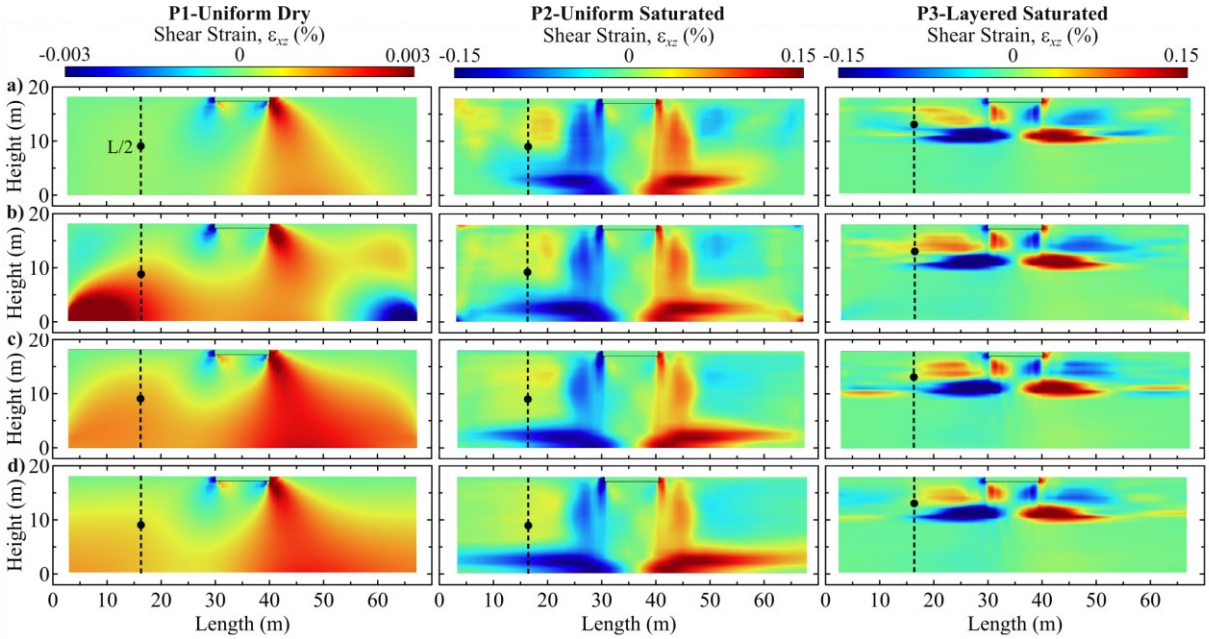

Figure 9. Contours of accumulated total shear strain at the end of shaking for all soil profiles (P1-P3) during M1, under the structure and in the far-field for the following boundary types and L/B = 2.7: a) rigid without DS; b) rigid with DS; c) FSB with periodic boundaries; and d) ILC.

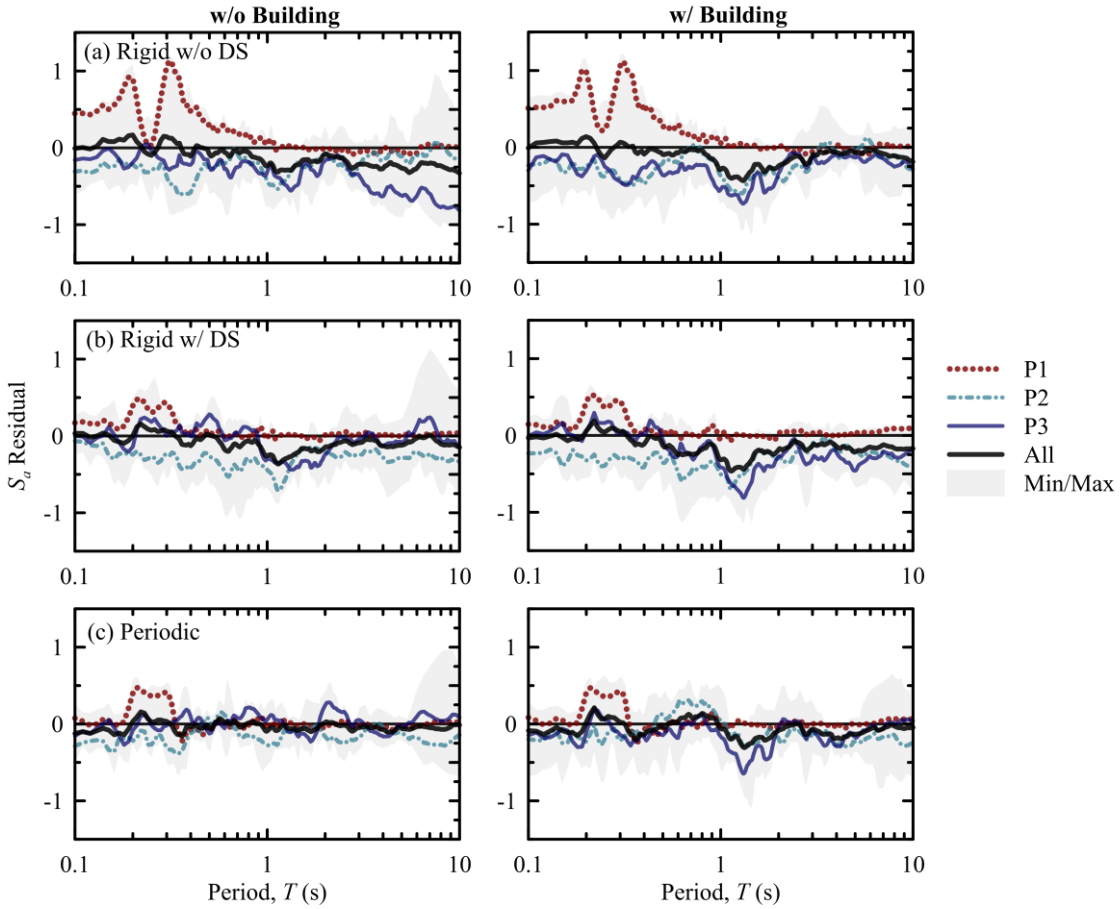

Figure 10. Comparison of the influence of lateral boundary type on average far-field spectral acceleration residuals relative to the ILC inside the following containers: a) rigid without DS; b) rigid with DS; and c) FSB with periodic boundaries, as a function of the soil profile type (P1-P3) in the middle of the liquefiable layer (or middle of dense layer for soil profile P1), with a building (right) at *L/2* distance from the foundation edge and without a building (left) in the center of the model during motions M1-M3. The gray shaded area outlines the minimum and maximum responses obtained from all analyses.

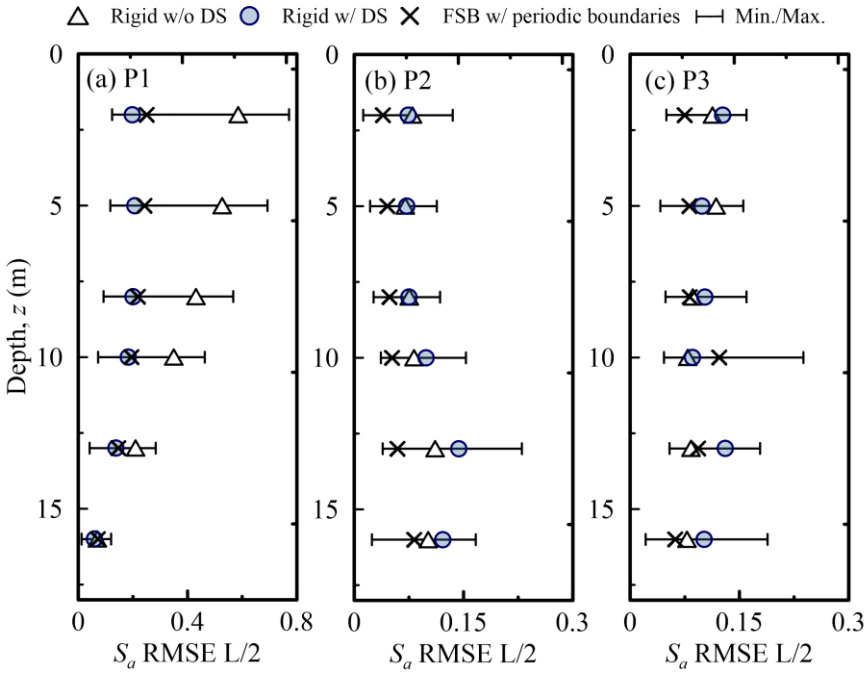

Figure 11. Comparison of RMSE of far-field spectral accelerations from T = 0.1-10 s as a function of depth and boundary type in models involving structures for soil profiles: a) P1; b) P2; and c) P3 during motion M1 at a distance of *L/2* from the foundation edge.

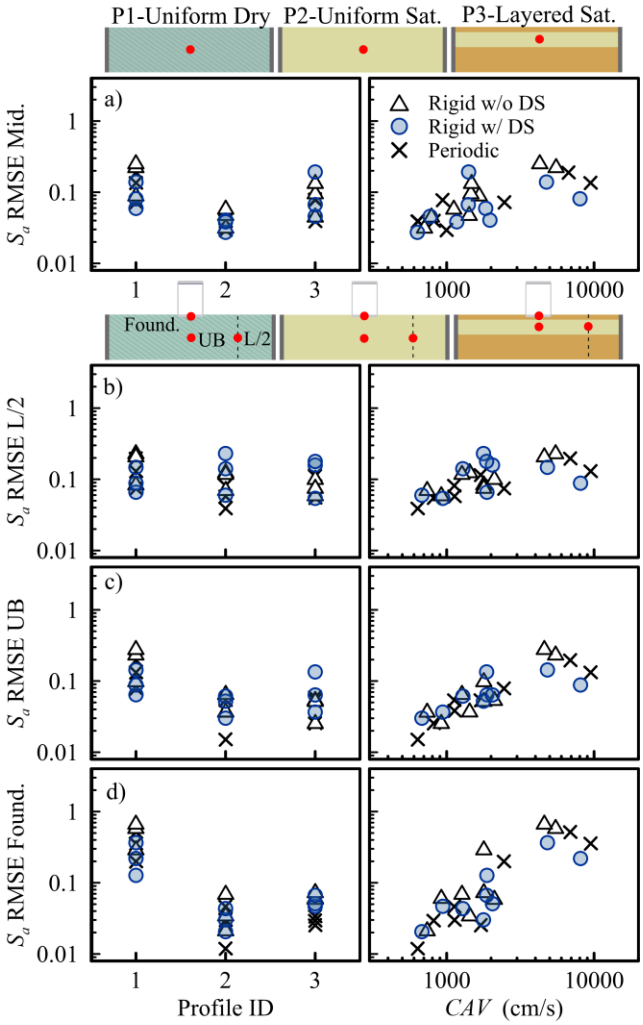

Figure 12. RMSE of spectral accelerations from $T = 0.1$-10 s as a function of soil profile type and the Cumulative Absolute Velocity (*CAV*) of the motion at the location of interest (as indicated by the red dots in the schematics): a) without a building at the center of the container; with a building: b) at a distance of *L/2* from the foundation edge in the middle of the liquefiable layer (or in the middle of the dense layer for soil profile P1); c) under the building (UB) in the middle of the liquefiable layer; and d) on the foundation.

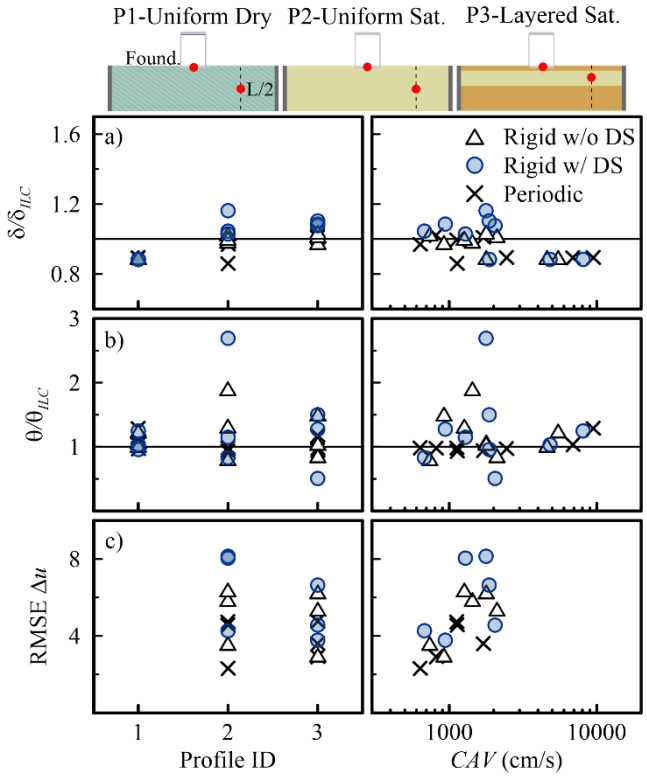

Figure 13. RMSE of: a) permanent foundation settlement (δ/δ_{ILC}); b) permanent foundation tilt (θ/θ_{ILC}) normalized by the ILC's response; and RMSE of excess pore water pressure (Δu) at a distance of $L/2$ from the foundation edge in the middle of the liquefiable layer as a function of soil profile type and the Cumulative Absolute Velocity (CAV) of the motion at the location of interest (as indicated by the red dots in the schematics).

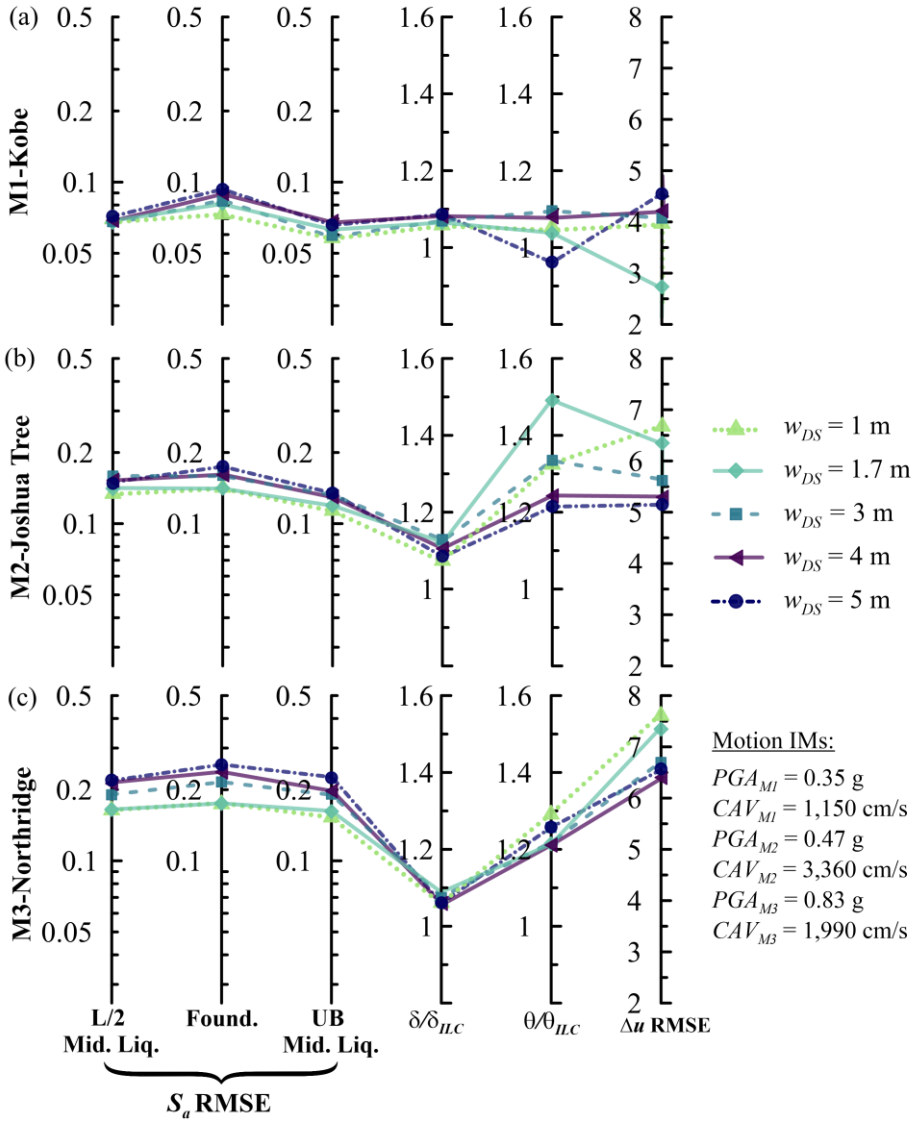

Figure 14. Comparison of seismic performance indices with different DS thicknesses (w_{DS}) for soil profiles: a) P1;b) P2; and c) P3, on the seismic performance indices, including the RMSE of spectral accelerations from T = 0.1-10 s [at $L/2$ and under the building (UB) in the middle of the liquefiable layer (or middle of the dense layer for soil profile P1), and at the foundation level], normalized permanent foundation settlement (δ/δ_{ILC}), permanent foundation tilt (θ/θ_{ILC}), and RMSE of excess pore water pressure (Δu) at a distance of $L/2$ from the foundation edge in the middle of the liquefiable layer.

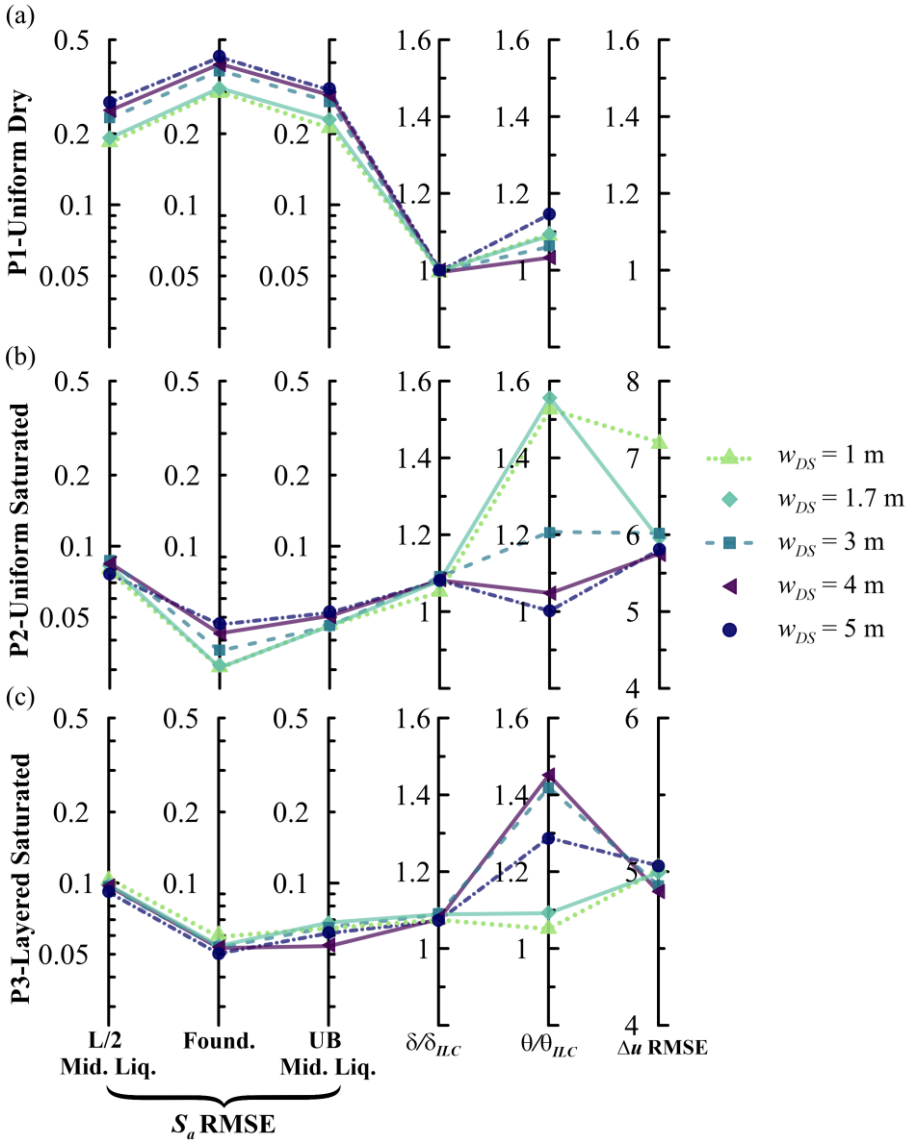

Figure 15. Comparison of seismic performance indices with different DS thicknesses (w_{DS}) for the motions: a) M1; b) M2; and c) M3, on the seismic performance indices, including the RMSE of spectral accelerations from T = 0.1-10 s [at *L/2* and under the building (UB) in the middle of the liquefiable layer (or middle of the dense layer for soil profile P1), and at the foundation level], normalized permanent foundation settlement (δ/δ_{ILC}), permanent foundation tilt (θ/θ_{ILC}), and RMSE of excess pore water pressure (Δu) at a distance of *L/2* from the foundation edge in the middle of the liquefiable layer.

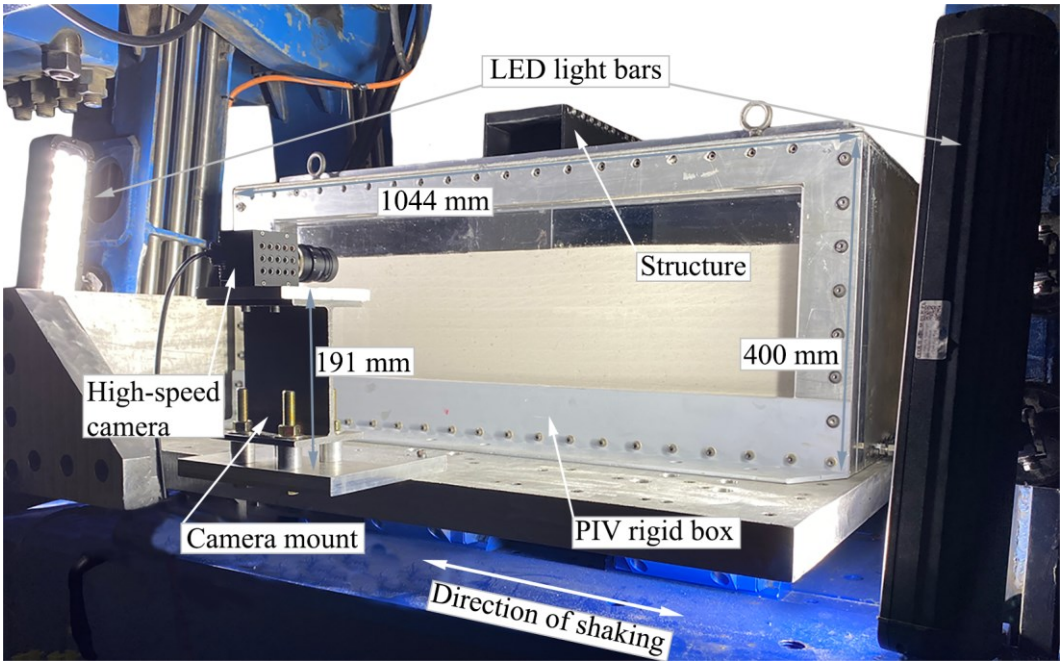

Figure 16. Photograph of the new high-speed deformation measurement system at CU Boulder (dimensions in model scale).

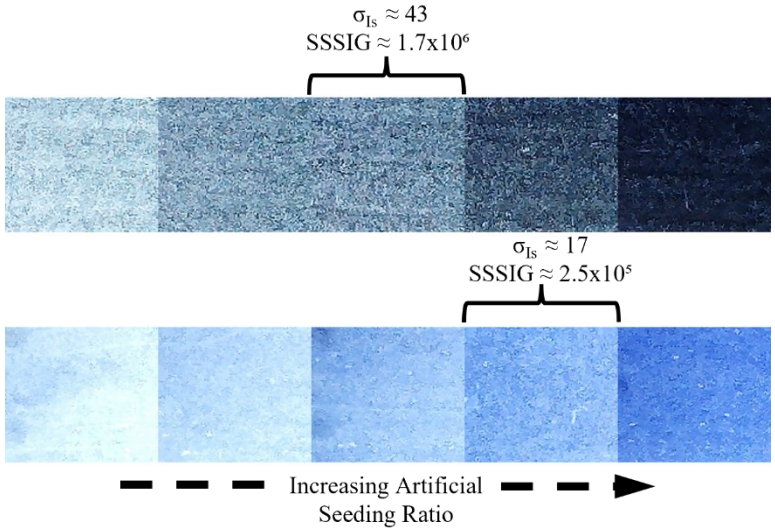

Figure 17. Representative range of ASRs observed in the texture-optimization process: (a) loose Ottawa sand seeded with dyed black sand; (b) dense Ottawa sand seeded with blue dyed sand. Standard deviation of subset pixel intensities, σ_{Is}, and the sum of squares of subset pixel intensity gradients (SSSIG) for example subsets (48 x 48 pixels) of chosen optimally-seeded sands.

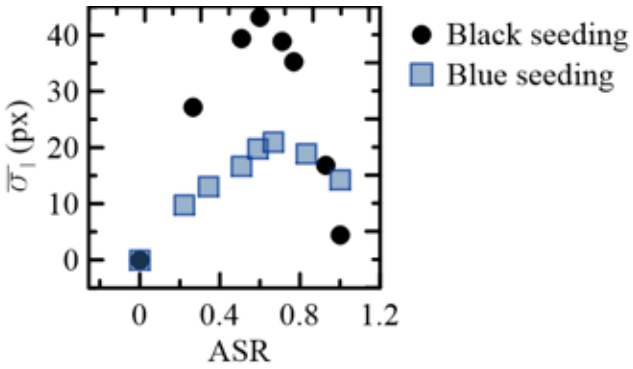

Figure 18. Artificial seeding ratio versus the mean standard deviation of pixel intensities due to the addition of seeding on Ottawa sand with blue (dense layer) and black (loose layer) dyed Ottawa sand.

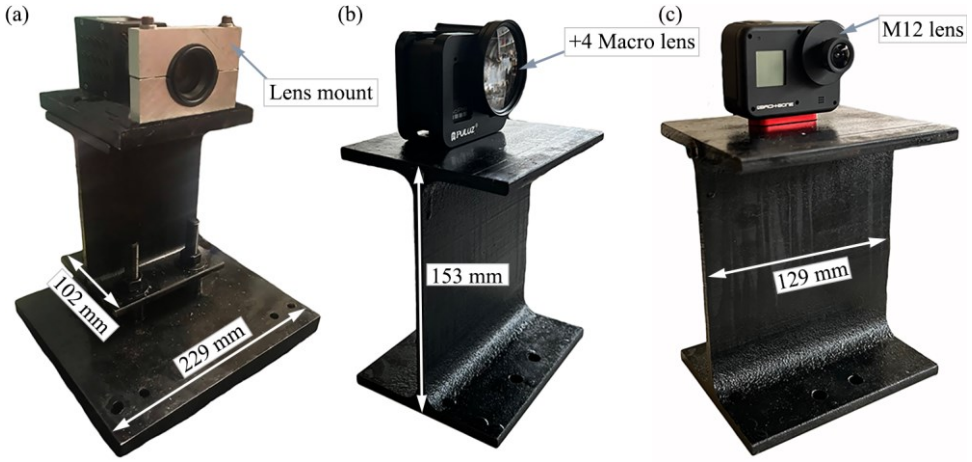

Figure 19. Photograph of cameras to be used for centrifuge experiments: (a) High-speed camera with lens and camera mount; (b) GoPro Hero8 with +4 Macro lens and protective case; (c) Back-bone modified GoPro Hero8 with M12 lens (all dimensions in model scale).

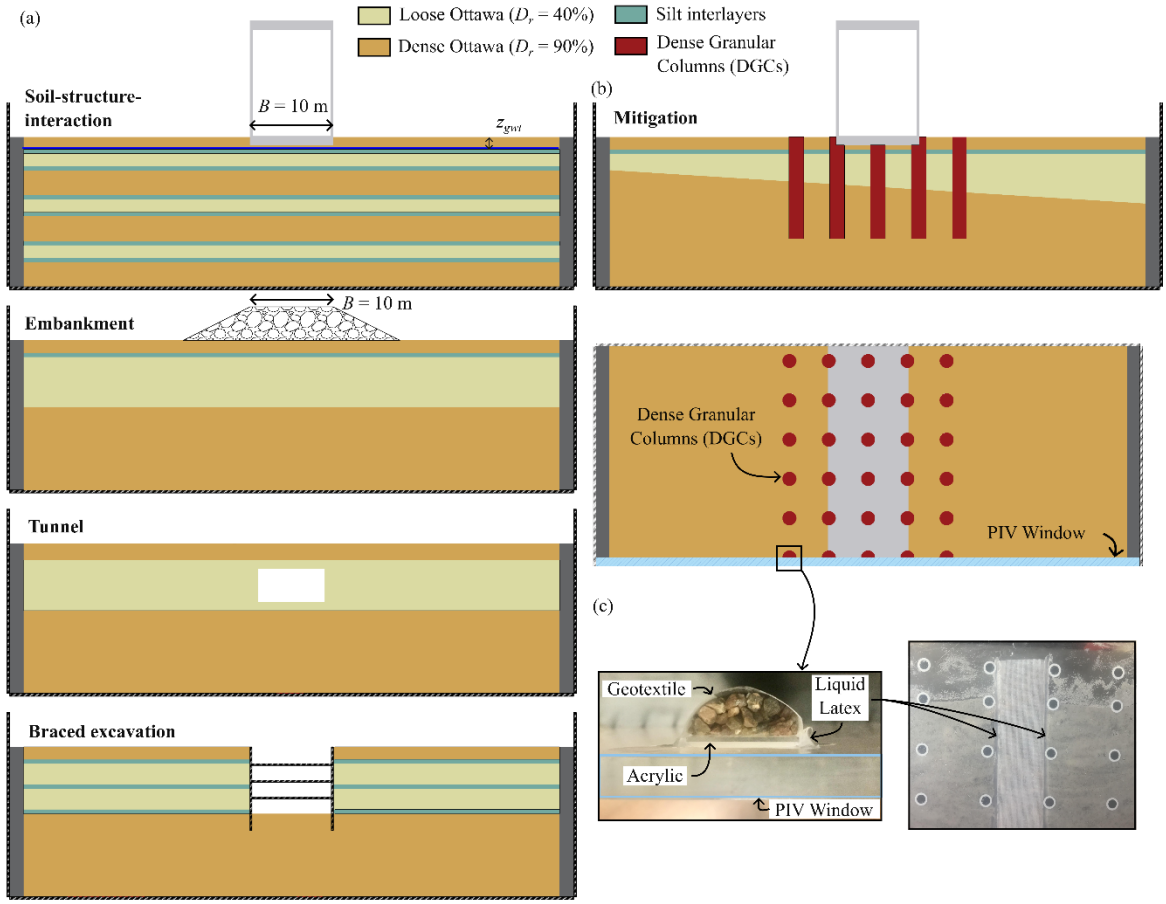

Figure 20. a) Configuration layout of potential applications of the designed experimental setup, b) DGC configuration with the SDOF structure in example application shown in elevation and plan views, c) Details of the DGC half-column configuration against the PIV window (all dimensions are in prototype scale meters).

Table 1. Properties of the target prototype structure and simplified model structure for centrifuge testing.

	Target structure in prototype scale	**Simplified model structure**	
		Prototype scale	**Model scale (N = 70)**
Number of stories	4	Equivalent SDOF	Equivalent SDOF
Seismic structural system	RCMF	RCMF[a]	RCMF[a]
Height above ground (m)	18.3	13.9	0.2
Footprint dimension (m)	10x25.34	10x25.34	0.143x0.362
Building weight (kN)	1.54×10^4	2.28×10^{4}[b]	0.0665
Foundation type	Strip footing	Strip footing	Strip footing
Foundation embedment (m)	1	1	0.014
Foundation contact pressure (kPa)	60.8	90	90
Fundamental Period (s)	0.64[c]	0.91[d]	0.87[e]

[a] Fabricated using Aluminum.
[b] Addition of LVDT holders, PVC barriers to prevent water intrusion, and available members led to a weight higher than the target design building.
[c] Design period according to ASCE 7-22; correspond to the lower bound of the range from Goel and Chopra (1997).
[d] Computed from eigen-value modal analyses in OpenSees.
[e] Found experimentally using a hammer impact test.

Table 2. Material properties used in numerical modeling of the container.

Material	**Young's modulus, *E* (MPa)**	**Poisson's ratio**	**Density (kg/m^3)**	**Material model**
Perspex	3210	0.37	1190	Elastic
Aluminum	69000	0.33	2700	Elastic

Table 3. Calibrated soil model parameters used for the PDMY02 constitutive model.

Description	**PDMY02 Ottawa sand**	
Relative density, D_r (%)	40	90
Sat. mass density, ρ_{sat} (kN/m^3)	1.94	2.03
Void ratio, e	0.7	0.55
Ref. effective confining pressure, P'_r (kPa)	101	101
Pressure dependence coeff., d	0.5	0.5
Octahedral reference low-strain shear modulus, G_{ref} (MPa)	82	105
Triaxial peak friction angle, ϕ'_{TXC} (°)	31	38.5
Phase transformation angle, ϕ_{pt} (°)	26.8	34
Control shear-induced volumetric change, contraction tendency based on dilation history, and overburden stress effects, respectively, c_1, c_2, c_3	0.61	0.076
	3.1	1.25
	2.24	1.36
Reflect dilation tendency, stress history, and overburden stress, respectively, d_1, d_2, and d_3	0.1	1.12
	3.0	3.0
	0.27	1.05
Number of yield surfaces generated by the model	20	20
Account for permanent shear strain (slip strain or cyclic mobility) in sloping ground, liq_1 and liq_2	1.0	1.0
	0.0	0.0

Table 4. Ground motion properties.

ID	Ground motion	Event	Station	Peak Ground Acceleration, *PGA* (g)	Significant Duration, $D_{5\text{-}95}$ (s)	Mean Period, T_m (s)	Cumulative Absolute Velocity, *CAV* (cm/s)	Arias Intensity, I_a (m/s)
M1	Kobe	1995 Kobe	Takatori	0.35	11.6	0.69	2.07	1,150
M2	Joshua	1992 Landers	Joshua Tree	0.47	26.3	0.56	8.64	3,360
M3	Northridge	1994 Northridge	Newhall-WPC	0.83	16.4	0.71	6.17	1,990

Table 5. Summary of key performance metrics for selected deformation measurement system

Reference	**Camera**	**Resolution**	**Sampling rate (fps)**
Cilingir and Madabhushi 2010	Vision Research Phantom v5.0	1024 x 1024	1000
Stanier and White 2013	Allied Vision Technologies Prosilica GC2450C	5 MP	15
Heron 2014	Motion Blitz EonSens Mini2	3 MP	523
		1280 x 1024	1155
Adamidis and Madabhushi 2017	Motion Blitz EonSens Mini2	1696 x 990	900
		1696 x 810	1108
		1696 x 500	1790
This investigation	CCM-1520	1440 x 1024	2000